

Hydromechanical Modeling of Unsaturated Flow in Double Porosity Media

Jinhyun Choo¹; Joshua A. White²; and Ronaldo I. Borja, A.M.ASCE³

Abstract: Geomaterials with aggregated structure or containing fissures often exhibit a bimodal pore size distribution that can be viewed as two coexisting pore regions of different scales. The double-porosity concept enables continuum modeling of such materials by considering two interacting pore scales satisfying relevant conservation laws. This paper develops a thermodynamically consistent framework for hydro-mechanical modeling of unsaturated flow in double-porosity media. With an explicit treatment of the two pore scales, conservation laws are formulated incorporating an effective stress tensor that is energy-conjugate to the rate of deformation tensor of the solid matrix. A constitutive framework is developed on the basis of energy-conjugate pairs identified in the first law of thermodynamics, which is then incorporated into a three-field mixed finite-element formulation for double-porosity media. Numerical simulations of laboratory- and field-scale problems are presented to demonstrate the impact of double porosity on the resulting hydromechanical responses. DOI: [10.1061/\(ASCE\)GM.1943-5622.0000558](https://doi.org/10.1061/(ASCE)GM.1943-5622.0000558). © 2016 American Society of Civil Engineers.

Author keywords: Coupled problem; Double porosity; Effective stress; Mixture theory; Unsaturated flow.

Introduction

Geomaterials with aggregated structure or containing fissures are abundant in natural formations and engineered systems. Soil aggregation is commonly encountered in nature, such as in the plough layer of tilled soils, in biologically active forest soils, and in humus-rich calcareous top soils (Šimůnek et al. 2003; Gerke 2006; Koliji et al. 2006, 2010b; Carminati et al. 2007; Jarvis 2007). It is also common in engineered geotechnical structures such as compacted soils and landfills (Fedá 1998; Li and Zhang 2009; Najser et al. 2010, 2012; Romero et al. 2011; Della Vecchia and Romero 2013; Musso et al. 2013; Burton et al. 2014). It is well recognized that all natural reservoir rocks possess fissures to some extent (Barenblatt et al. 1960; Warren and Root 1963; Kazemi et al. 1976; Moench 1984; Lewandowska and Auriault 2013; Katsuki et al. 2014; Vu et al. 2014; Bennett et al. 2015), and additional fissures may be induced by engineering activities (Abousleiman et al. 2014; Carneiro 2009; Weng et al. 2011; Foster and Mohammad Nejad 2013; Lamb et al. 2013; Li et al. 2013; Rahman and Rahman 2013a, b; Mohammadnejad and Khoei 2013; Zhang et al. 2015; Yin 2013; White et al. 2014; Tjioe and Borja 2015). Fissures have been observed in a variety of natural soils as well (Hu et al. 2013; Vitone et al. 2013a, b). These distinctive features challenge the performance of important infrastructure and modeling multiphysical processes that could have serious implications for hazard mitigation and environmental protection (Borja and White 2010b; Borja et al.

2012a, b; Liu et al. 2014; Raj and Sengupta 2014; Rotisciani et al. 2015).

Aggregated soils or fissured rocks often exhibit a bimodal pore size distribution that can be treated as a composite with two coexisting pore regions of different scale (Li and Zhang 2009; Romero et al. 2011; Hall et al. 2013; Burton et al. 2014). Because of the significant difference in their pore sizes, the two regions exhibit markedly different hydromechanical characteristics (Koliji et al. 2006, 2008, 2010a; Frey et al. 2013; Shen et al. 2014). In aggregated soils, for example, the inter-aggregate pores serve as conduits for small-scale preferential, non-equilibrium flow, whereas the intra-aggregate pores and the contact surface areas between the aggregates can provide pathways for fluid migration (Šimůnek et al. 2003; Gerke 2006; Jarvis 2007; Yang et al. 2014). Fissures in rocks govern preferential flow patterns, but the matrix pores can trap and transport a substantial amount of pore fluids as well (Barenblatt et al. 1960; Warren and Root 1963; Moench 1984). One of the major challenges in modeling materials with two dominant pore scales is how to accurately capture the processes taking place in each scale without resorting to brute force calculations.

The double-porosity concept enables continuum modeling of materials with two pore scales. Here, the term *double porosity* is used to indicate a framework in which two pore regions overlap within the solid matrix. Throughout the paper, the term *macropores* refers to the larger pore scale (e.g., inter-aggregate pores or fissures), and *micropores* refers to the smaller pore scale (e.g., intra-aggregate pores or matrix pores). Fig. 1 shows a schematic representation of a mixture with double porosity. Broadly speaking, there are two types of material with double porosity (Šimůnek et al. 2003). The first is a *dual-porosity* material, in which the pore fluids could flow through the macropores only but are trapped within the micropores. However, experimental evidence suggests that in some materials, such as aggregated soils, the pore fluids could also migrate within the micropores (Šimůnek et al. 2003; Gerke 2006; Carminati et al. 2007; Jarvis 2007). The term *dual permeability* is used for this latter type of material, in which the pore fluid could migrate through the macropores as well as within the micropores. In this paper, the term *double porosity* is used in the context of dual permeability.

¹Ph.D. Candidate, Dept. of Civil and Environmental Engineering, Stanford Univ., Stanford, CA 94305.

²Research Scientist, Atmospheric, Earth, and Energy Division, Lawrence Livermore National Laboratory, Livermore, CA 94551.

³Professor, Dept. of Civil and Environmental Engineering, Stanford Univ., Stanford, CA 94305 (corresponding author). E-mail: borja@stanford.edu

Note. This manuscript was submitted on September 19, 2014; approved on June 16, 2015; published online on January 28, 2016. Discussion period open until June 28, 2016; separate discussions must be submitted for individual papers. This paper is part of the *International Journal of Geomechanics*, © ASCE, ISSN 1532-3641.

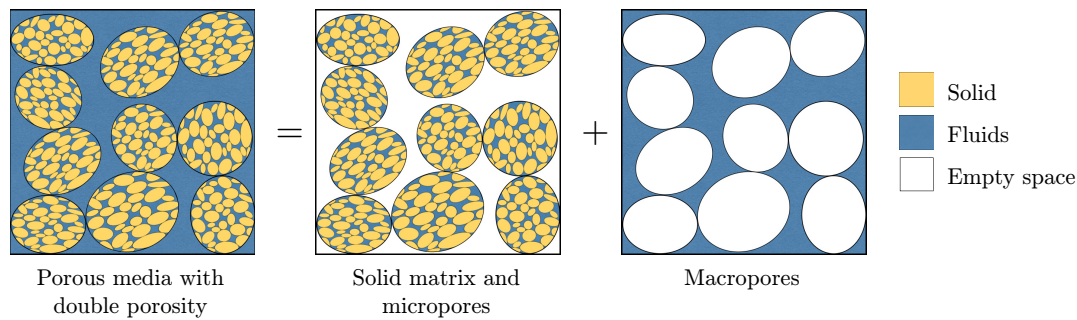


Fig. 1. Schematic representation of a mixture with double porosity

Double porosity is a framework widely used in petroleum engineering and subsurface hydrology for various flow problems. The concept was first proposed by Barenblatt et al. (1960) to tackle the anomalous flow through fissured rocks in reservoirs and aquifers (Warren and Root 1963; Kazemi et al. 1976; Moench 1984; Berkowitz et al. 1988; Zimmerman et al. 1993). It was later applied for explaining fluid flow in aggregated soils (Gerke and van Genuchten 1993a; Lewandowska et al. 2004, 2005, 2008). Recent studies have extended its applications to biological and engineered materials with similar pore scale characteristics (Gauden et al. 2007; Venegas and Umnova 2011; Rohan et al. 2012; Svanadze and Scalia 2013). Although several previous studies have adopted the double-porosity framework for coupled solid deformation and fluid flow in porous media (Elsworth and Bai 1992; Lewis and Ghafouri 1997; Callari and Federico 2000; Khalili and Selvadurai 2003; Zhang and Roegiers 2005; Koliji et al. 2010a; Mašin 2013), there has been significant disagreement in the theoretical formulation of the problem, particularly with the definition of effective stress. The purpose of the work presented in this paper is to develop a rigorous and consistent formulation for coupled hydromechanical modeling of unsaturated porous media with double porosity.

There are two major challenges in developing a theoretical framework for hydromechanical modeling of double-porosity media. The first challenge is defining the effective stress to accommodate two pore pressure degrees of freedom emanating from the two scales. The second challenge is developing a constitutive framework that captures all the important poromechanical processes at the two pore scales. In this work, the first law of thermodynamics is used to address these two challenges, motivated by the work by Borja (2004, 2006) and Song and Borja (2014b) for unsaturated porous media with single porosity.

Energy-conjugate pairs in the first law of thermodynamics suggest groupings of variables that must be linked via constitutive relations. This is because the same energy-conjugate pairs will appear in the dissipation inequality, and the standard Coleman-Noll procedure will yield that all variables involved in a non-dissipative energy-conjugate pair should be related by a constitutive law to ensure non-negative entropy production (i.e., the second law of thermodynamics). As such, identifying energy-conjugate pairs has proven useful to gain insight into constitutive modeling of multiphase porous media. For instance, energy conjugacy between the effective stress tensor and the rate of deformation tensor of the solid matrix suggests that a mechanical constitutive law must be established in terms of the effective stress, rather than the total stress, or the net stress, or some other measure of stress. A thermodynamically consistent effective stress could lead to many desirable results, including the fact that, when reckoned with respect to this stress, the position of the critical state line is

demonstrably unique (Nuth and Laloui 2008). For double-porosity media, Borja and Koliji (2009) derived an effective stress tensor that is energy-conjugate to the rate of deformation tensor for the solid matrix with double-porosity. By inspecting how the variables are paired in the expression for the rate of change of internal energy, they also identified other constitutive relations for double-porosity media. The constitutive relations of interest in this work concern not only the mechanical laws but also those emanating from fluid flow and coupled hydromechanical processes occurring at the two pore scales.

The present work develops a thermodynamically consistent framework for hydromechanical modeling of double-porosity media in which the pores are assumed to be filled with water and air. Thermodynamic consistency is achieved by making use of the aforementioned approaches for the effective stress and multiphysical constitutive relations at the two pore scales. To the authors' knowledge, this is the first time that a poromechanical framework for double-porosity media has been developed from direct application of the principles of thermodynamics. Essential ingredients for coupling unsaturated flow with deformation of the solid matrix having two pore scales are presented in this paper. Without loss of generality, the theory is developed under the assumption of infinitesimal deformation, and the treatment of finite-deformation effects are deferred for future publication.

This paper is organized as follows. Conservation laws for double-porosity media are first formulated incorporating a thermodynamically consistent effective stress tensor. A constitutive framework is then developed on the basis of energy-conjugate pairs identified in the first law of thermodynamics. Subsequently, a three-field mixed finite-element formulation is developed for the numerical solution of fully coupled flow and deformation problems. Numerical examples are presented to demonstrate the impact of double porosity on the hydromechanical responses of a laboratory-scale specimen and a field-scale slope problem.

Conservation Laws

In this section, the balance of mass and balance of linear momentum for double-porosity media are formulated by distinguishing between the macropore and micropore pressures and by using a thermodynamically consistent effective stress. Also presented is an expression for the rate of change of internal energy that will prove to be useful for developing other relevant constitutive relations.

Balance of Mass

Consider a mixture of solid, water, and air, in which the solid forms a matrix with two dominant pore scales. The volume fractions are defined in the usual way

$$\phi^s = dV_s/dV, \quad \phi^{i\alpha} = dV_{i\alpha}/dV, \quad i = M, m, \quad \alpha = a, w \quad (1)$$

where index s = solid phase; index i = either the macropore (M) or the micropore (m); and index α = pore fluid phase that can be either water (w) or air (a). Indices are used as superscript characters when referring to partial properties of a constituent (e.g., volume fractions) and as superscript characters when referring to intrinsic properties (e.g., constituent volumes). Volume fractions satisfy the closure relation

$$\phi^s + \sum_{i=M,m} \sum_{\alpha=w,a} \phi^{i\alpha} = 1 \quad (2)$$

Partial mass densities (e.g., ρ^s) can be expressed in terms of the intrinsic mass densities (e.g., ρ_s) and volume fractions via relations of the form

$$\rho^s = \phi^s \rho_s, \quad \rho^{i\alpha} = \phi^{i\alpha} \rho_{\alpha}, \quad i = M, m, \quad \alpha = a, w \quad (3)$$

The total mass density of the mixture (ρ) is obtained by summing all of the partial mass densities

$$\rho = \rho^s + \sum_{i=M,m} \sum_{\alpha=w,a} \rho^{i\alpha} \quad (4)$$

Pore fractions define the portions of the total pore volume occupied by the two dominant pore regions

$$\psi^i = \frac{\phi^i}{1 - \phi^s}, \quad i = M, m \quad (5)$$

where $\phi^i = \phi^{iw} + \phi^{ia}$, which yields the closure condition

$$\psi^M + \psi^m = 1 \quad (6)$$

Accordingly, the local water saturation at pore scale i is given by the relation

$$S^i = \frac{\phi^{iw}}{\phi^i} = \frac{\phi^{iw}}{\psi^i(1 - \phi^s)}, \quad i = M, m \quad (7)$$

which can be thought of as the local degree of saturation at each of the two pore scales. The global (or overall) degree of saturation can then be calculated as

$$S = \sum_{i=M,m} \frac{\phi^{iw}}{1 - \phi^s} = \sum_{i=M,m} \psi^i S^i \quad (8)$$

Without loss of generality and for simplicity, in the following developments, water is assumed to be incompressible and the pore air pressure is assumed to be zero (i.e., atmospheric). These assumptions are realistic for near-surface soil formation applications and can easily be rectified with the introduction of fluid compressibility and the pore air variables for more general multiphysics applications.

The balance of mass for pore water in the macropores and micropores, accommodating for the mass transfer term between the two pore scales, can be expressed as follows [with a minor correction from Borja and Koliji (2009)]:

$$\phi^i \dot{S}^i + S^i \psi^i B \nabla \cdot \mathbf{v} + \nabla \cdot \mathbf{q}_i = \frac{1}{\rho_i} c^i, \quad i = M, m \quad (9)$$

where the superimposed dot denotes a material time derivative following the solid motion; B = Biot coefficient; \mathbf{v} = solid velocity; $\mathbf{q}_i = \phi^{iw} \tilde{\mathbf{v}}_i$ = seepage (Darcy) velocities of pore water in the macropores and micropores; and $\tilde{\mathbf{v}}_i = \mathbf{v}_i - \mathbf{v}$ = relative velocity of pore water at pore scale i . The water mass transfer terms are represented by c^i appearing on the right-hand side, which satisfies the closure condition $c^M + c^m = 0$.

Balance of Linear Momentum

The balance of linear momentum can be expressed in terms of an effective stress tensor derived by Borja and Koliji (2009), which takes the form

$$\boldsymbol{\sigma}' = \boldsymbol{\sigma} + B\bar{p}\mathbf{1} \quad (10)$$

where $\boldsymbol{\sigma}$ and $\boldsymbol{\sigma}'$ = total and effective Cauchy stress tensor; $\mathbf{1}$ = second-order identity tensor; and \bar{p} = mean pore pressure given by

$$\bar{p} = \sum_{i=M,m} [\psi^i S^i p_i + \psi^i (1 - S^i) p_{ia}] \quad (11)$$

where p_i and p_{ia} = pore water pressure and pore air pressure at pore scale i (the index w for the pore water pressure is dropped for simplicity). Note that the formulation uses the standard mechanics notation where stress is positive in tension and pressure is positive in compression. For the case of passive air pressure (i.e., zero pore air pressure), the preceding expression simplifies to the form

$$\bar{p} = \sum_{i=M,m} \psi^i S^i p_i \quad (12)$$

In other words, the effective stress tensor $\boldsymbol{\sigma}'$ can be obtained from taking the mean pore pressure (\bar{p}) that is weighted according to the pore fractions and local degrees of saturation of the two pore scales. Under special conditions, this effective stress reduces to some well-known effective stresses. For example, for single-porosity media (i.e., either $\psi^M = 1$ or $\psi^m = 1$), this effective stress reduces to the form for single-porosity continua developed by Borja (2006). If the pores are completely saturated with water, it specializes to the effective stress tensor investigated by Nur and Byerlee (1971). Finally, if the Biot coefficient is $B = 1$, then one recovers the Terzaghi effective stress (Terzaghi 1943).

The balance of linear momentum for the entire mixture takes the following form (Borja and Koliji 2009; Borja 2014):

$$\nabla \cdot (\boldsymbol{\sigma}' - \bar{p}\mathbf{1}) + \rho \mathbf{g} = \bar{\mathbf{c}} \quad (13)$$

where \mathbf{g} = gravity acceleration vector; and $\bar{\mathbf{c}}$ = momentum produced by the mass transfer of water between the two pore scales, which takes the form

$$\bar{\mathbf{c}} = \sum_{i=M,m} c^i \tilde{\mathbf{v}}_i \quad (14)$$

Here, the closure condition $c^M + c^m = 0$ causes the solid velocity terms to cancel out from their original form given by Borja and Koliji (2009).

Balance of Internal Energy

An expression for the rate of change of internal energy for a solid–fluid mixture with double porosity was presented in Eq. (76) of Borja and Koliji (2009). The following equation is a simplified

version of this expression that accounts for mechanical powers only (signs of some terms are corrected from the original expression):

$$\begin{aligned} \rho \dot{e} = & \boldsymbol{\sigma}' : \mathbf{d} + \sum_{i=M,m} \tilde{\mathbf{v}}_i \cdot \nabla(\phi^{iw})p_i - \sum_{i=M,m} \psi^i(1 - \phi^s)s_i S^i \\ & - \sum_{i=M,m} c^i \left(p_i - \frac{1}{2} \tilde{\mathbf{v}}_i \cdot \tilde{\mathbf{v}}_i \right) - (1 - \phi^s) \pi \dot{\psi}^m \end{aligned} \quad (15)$$

where \dot{e} = rate of change of internal energy per unit total mass of the mixture; \mathbf{d} = rate of deformation tensor of the solid matrix; s_i = local suction at pore scale i , defined as $s_i = -p_i$; and π = difference between the mean pressures at the macropores and micropores, $\pi = S^M p_M - S^m p_m$. To highlight the pairings of the constitutive variables implied by this preceding expression, Eq. (15) is rewritten in a more abstract form as

$$\begin{aligned} \rho \dot{e} = & \langle \boldsymbol{\sigma}', \mathbf{d} \rangle + \sum_{i=M,m} \langle \tilde{\mathbf{v}}_i, \phi^{iw}, p_i \rangle - \sum_{i=M,m} \langle \psi^i, (1 - \phi^s), s_i, S^i \rangle \\ & - \sum_{i=M,m} \langle c^i, p_i, \tilde{\mathbf{v}}_i \rangle - \langle (1 - \phi^s), \pi, \dot{\psi}^m \rangle \end{aligned} \quad (16)$$

where the symbol $\langle \circ, \dots, \circ \rangle$ denotes energy conjugacy. This expression for the rate of change of internal energy yields five groups of constitutive variables, suggesting that five constitutive relations must be established relating these variables. Three of these constitutive relations (the terms with the summation) are defined separately at each pore scale. Specific constitutive models for these energy-conjugate pairs are proposed in the following section.

Constitutive Framework

Guided by the pairings identified in Eq. (16), constitutive laws are now introduced to close the boundary value problem. The first pair on the right-hand side of this equation suggests a constitutive law for the solid matrix of the form

$$\boldsymbol{\sigma}' = \mathbb{C} : \dot{\boldsymbol{\epsilon}} \quad (17)$$

where \mathbb{C} = fourth-order tangent tensor that may be obtained, for example, from an elastoplastic constitutive law; and $\boldsymbol{\epsilon}$ = infinitesimal strain tensor of which rate $\dot{\boldsymbol{\epsilon}}$ is equivalent to the rate of deformation tensor \mathbf{d} for infinitesimal deformation. The reduced dissipation inequality formulated in Eq. (83) of Borja and Koliji (2009) suggests that a yield function of an unsaturated double-porosity material may depend on the suctions at the macropores and micropores. However, because of the absence of firm experimental evidence, incorporating the effect of two-scale suctions to elastoplasticity, similar to what was done for single-porosity modeling (e.g., Borja 2004; Borja et al. 2013b; Liu and Muraleetharan 2012a, b; Song and Borja 2014a), is not pursued here.

The second pair suggests a constitutive relation among the relative flow vector, volume fraction, and pore water pressure at each pore scale. Noting that $\mathbf{q}_i = \phi^{iw} \tilde{\mathbf{v}}_i$, this is equivalent to a relation between the seepage velocity and the pore pressure at pore scale i . Under the assumptions of laminar flow and isotropic media, it is postulated that Darcy's law is valid for the two pore scales. The seepage velocities of pore water in the macropores and micropores are then given by

$$\mathbf{q}_{iw} = -k_{ri} \frac{k_i}{\mu_w} \cdot (\nabla p_i - \rho_w \mathbf{g}), \quad i = M, m \quad (18)$$

where k_{ri} and k_i = relative and intrinsic permeabilities at pore scale i ; and μ_w = dynamic viscosity of water. The relative permeability depends on the local degree of saturation and is elaborated further later. Note that porosity may also vary with finite deformation (Song and Borja 2014a, b), although it is considered constant in the present infinitesimal formulation.

The third pair in the internal energy equation suggests a relation among the local matric suction (s_i) and the local degree of saturation (S^i) for a given volume fraction. This work uses the well-known van Genuchten equation (van Genuchten 1980) at each pore scale, which is written as

$$S^i(s_i) = S_1^i + (S_2^i - S_1^i) [1 + (s_i/s_{\alpha i})^{n_i}]^{-m_i}, \quad i = M, m \quad (19)$$

where S_1^i and S_2^i = residual water saturation and maximum water saturation at pore scale i , respectively; $s_{\alpha i}$ = scaling suctions; and n_i and m_i = parameters that determine the shape of the water retention curves. Note that the fitting parameter m_i is related to the parameter n_i according to the relation

$$m_i = 1 - 1/n_i \quad (20)$$

The relative permeabilities of the water phase in the macropores and micropores are given, respectively, by

$$k_{ri} = \theta^{1/2} [1 - (1 - \theta_i^{1/m_i})^{m_i}]^2, \quad \theta_i = \frac{S^i - S_1^i}{S_2^i - S_1^i}, \quad i = M, m \quad (21)$$

Although water retention curves can be developed quite easily for the entire porous material, they are quite challenging to develop for each of the two pore scales. To develop water retention curves appropriate for the macropores and micropores, one can resort to an indirect approach, as used in some previous studies (Durner 1994; Buscarera and Einav 2012; Casini et al. 2012). The idea is to superimpose two water retention curves, one for the micropores and the other for the macropores, and calibrate the overall curve with the global water retention data, recalling that the global saturation can be calculated from the weighted average of the local suctions, as shown in Eq. (8). Another approach is to ignore suction in the macropores because of their much lower air-entry value, as done by Koliji et al. (2010a). However, when the suction in the macropores is not negligible, such as what the experimental results of Romero et al. (1999, 2011) suggest, the latter approach may lead to oversimplification. Last, it is noted that, in some cases, the changes in the pore volume could have a significant impact on the water retention curves of double-porosity media [see Romero et al. (2011) and Della Vecchia et al. (2015) for some experimental evidence] and single-porosity media (Gallipoli et al. 2003; Miller et al. 2008). In the finite-deformation range, this relationship must be considered whenever experimental data permit.

The fourth pair involves mass transfer terms (c^i) that are new to the formulation (i.e., relative to the one presented by Borja and Koliji 2009). For obvious reason, these terms do not enter into the formulation for a single-porosity problem. Note that the terms p and $\tilde{\mathbf{v}}$ have already been related by Darcy's law; thus, one can eliminate the relative velocity term and simply link c and p by an appropriate constitutive law. Also, because of the closure condition $c^M = -c^m$, one can interpret the constitutive law as relating the diffusive mass transfer term to the pressure difference at the two pore scales. In

fact, a vast number of studies have advanced constitutive relations of this form (e.g., see Warren and Root 1963; Dykhuizen 1987, 1990; Gerke and van Genuchten 1993b; Haggerty and Gorelick 1995; Köhne et al. 2004; Sarma and Aziz 2006). Among them, a first-order mass transfer equation of the following form is common:

$$c^M = \frac{\bar{\alpha}}{\mu_w} (p_m - p_M), \quad c^m = \frac{\bar{\alpha}}{\mu_w} (p_M - p_m) \quad (22)$$

where $\bar{\alpha}$ = dimensionless parameter that depends on the characteristics of the interface between the macropores and micropores, such as permeability, spacing, and shape. Several specific forms of the parameter $\bar{\alpha}$ have been suggested on the basis of theoretical and experimental results (e.g., Warren and Root 1963; Dykhuizen 1990; Gerke and van Genuchten 1993b). This study uses an equation proposed by Gerke and van Genuchten (1993b), given by

$$\bar{\alpha} = \bar{k} \frac{\beta}{a^2} \gamma \quad (23)$$

where \bar{k} = interface permeability; a = characteristic length of the macropore spacing; β = dimensionless coefficient that accounts for macropore geometry; and γ = dimensionless scaling coefficient that was shown to be 0.4 to fit experimental results. Similar to the constitutive relations developed for the other groups, which are not unique, one can explore other possible constitutive laws for the diffusive mass transfer term that better fit the experimental data.

The final pair in the expression for the rate of change of internal energy suggests a constitutive relationship between the mean pore pressure difference and the macropore volume fraction. As noted by Borja and Koliji (2009), this is an open question particularly in the finite-deformation range, where the macropore volume fraction may change significantly. For the infinitesimal theory, where the volume fractions may not change significantly (i.e., $\psi^m \approx 0$), it is reasonable to ignore this yet undetermined constitutive relation.

Mixed Finite-Element Formulation

This section formulates a three-field mixed finite-element solution to an initial boundary value problem of coupled solid deformation and fluid diffusion with double porosity. Strong and weak forms are first presented on the basis of the theoretical developments described in the previous section. Then, a three-field matrix form is developed for solving initial boundary value problems.

Strong Form

Consider a closed domain denoted by $\bar{\Omega} = \Omega \cup \Gamma$, where Ω is an open domain and Γ is the boundary of Ω . The boundary Γ is assumed to be suitably decomposed as follows: displacement and traction boundaries for solid, Γ_u and Γ_t , respectively; pressure and flux boundaries for water in the macropores, Γ_{p_M} and Γ_{q_M} , respectively; and pressure and flux boundaries for water in the micropores, Γ_{p_m} and Γ_{q_m} , respectively. The boundaries are subject to the following set relations:

$$\Gamma = \overline{\Gamma_u \cup \Gamma_t} \quad \text{and} \quad \emptyset = \Gamma_u \cap \Gamma_t \quad (24)$$

$$\Gamma = \overline{\Gamma_{p_M} \cup \Gamma_{q_M}} \quad \text{and} \quad \emptyset = \Gamma_{p_M} \cap \Gamma_{q_M} \quad (25)$$

$$\Gamma = \overline{\Gamma_{p_m} \cup \Gamma_{q_m}} \quad \text{and} \quad \emptyset = \Gamma_{p_m} \cap \Gamma_{q_m} \quad (26)$$

where \emptyset = null set and the overline denotes a closure.

The strong form of the initial boundary value problem can be stated as follows. Given $\hat{\mathbf{u}}$, $\hat{\mathbf{t}}$, \hat{p}_M , \hat{q}_M , \hat{p}_m , and \hat{q}_m , find \mathbf{u} , p_M , and p_m such that

$$\nabla \cdot (\boldsymbol{\sigma}' - \bar{p}\mathbf{1}) + \rho \mathbf{g} = \bar{\mathbf{c}} \quad (27)$$

and

$$\phi^i S^i + S^i \psi^i B \nabla \cdot \mathbf{v} + \nabla \cdot \mathbf{q}_i = \frac{1}{\rho_i} c^i, \quad i = M, m \quad (28)$$

subject to boundary conditions

$$\mathbf{u} = \hat{\mathbf{u}} \quad \text{on} \quad \Gamma_u \quad (29)$$

$$\mathbf{n} \cdot \boldsymbol{\sigma} = \hat{\mathbf{t}} \quad \text{on} \quad \Gamma_t \quad (30)$$

$$p_M = \hat{p}_M \quad \text{on} \quad \Gamma_{p_M} \quad (31)$$

$$-\mathbf{n} \cdot \mathbf{q}_M = \hat{q}_M \quad \text{on} \quad \Gamma_{q_M} \quad (32)$$

$$p_m = \hat{p}_m \quad \text{on} \quad \Gamma_{p_m} \quad (33)$$

$$-\mathbf{n} \cdot \mathbf{q}_m = \hat{q}_m \quad \text{on} \quad \Gamma_{q_m} \quad (34)$$

and initial conditions

$$\mathbf{u} = \mathbf{u}_0, \quad p_M = p_{M0}, \quad p_m = p_{m0} \quad (35)$$

for all $(\mathbf{x}, t) \in (\bar{\Omega} \times t = 0)$. Here, symbols with the hat denote the prescribed boundary conditions, $\hat{\mathbf{t}}$ is the prescribed traction vector.

Weak Form

To develop the weak form of the problem, the spaces of trial functions are defined as

$$S_u = \{\mathbf{u} | \mathbf{u} \in H^1, \mathbf{u} = \hat{\mathbf{u}} \quad \text{on} \quad \Gamma_u\} \quad (36)$$

$$S_{p_M} = \{p_M | p_M \in H^1, p_M = \hat{p}_M \quad \text{on} \quad \Gamma_{p_M}\} \quad (37)$$

$$S_{p_m} = \{p_m | p_m \in H^1, p_m = \hat{p}_m \quad \text{on} \quad \Gamma_{p_m}\} \quad (38)$$

where H^1 is a Sobolev space of order 1. Corresponding spaces of weighting functions are also defined by imposing homogeneous conditions on the Dirichlet boundaries

$$\mathcal{V}_u = \{\boldsymbol{\eta} | \boldsymbol{\eta} \in H^1, \boldsymbol{\eta} = \mathbf{0} \quad \text{on} \quad \Gamma_u\} \quad (39)$$

$$\mathcal{V}_{p_M} = \{\omega_M | \omega_M \in H^1, \omega_M = 0 \quad \text{on} \quad \Gamma_{p_M}\} \quad (40)$$

$$\mathcal{V}_{p_m} = \{\omega_m | \omega_m \in H^1, \omega_m = 0 \quad \text{on} \quad \Gamma_{p_m}\} \quad (41)$$

The weak form of the problem may be stated as follows. Find $\{\mathbf{u}, p_M, p_m\} \in \mathcal{S}_u \times \mathcal{S}_{p_M} \times \mathcal{S}_{p_m}$ such that, for all $\{\boldsymbol{\eta}, \omega_M, \omega_m\} \in \mathcal{V}_u \times \mathcal{V}_{p_M} \times \mathcal{V}_{p_m}$, the following equations are satisfied:

1. Balance of linear momentum

$$\int_{\Omega} \nabla^s \boldsymbol{\eta} : (\boldsymbol{\sigma}' - B\bar{p} \mathbf{1}) d\Omega = \int_{\Omega} \boldsymbol{\eta} \cdot (\rho \mathbf{g} + \bar{\mathbf{c}}) d\Omega + \int_{\Gamma_t} \boldsymbol{\eta} \cdot \hat{\mathbf{t}} d\Gamma \quad (42)$$

2. Balance of mass in the macropores

$$\begin{aligned} \int_{\Omega} \omega_M \phi^M \dot{S}^M d\Omega + \int_{\Omega} \omega_M S^M \psi^M B \nabla \cdot \mathbf{v} d\Omega - \int_{\Omega} \nabla \omega_M \cdot \mathbf{q}_M d\Omega \\ = -\frac{1}{\rho_i} \int_{\Omega} \omega_M c^M d\Omega + \int_{\Gamma_{q_M}} \omega_M \hat{q}_M d\Gamma \end{aligned} \quad (43)$$

3. Balance of mass in the micropores

$$\begin{aligned} \int_{\Omega} \omega_m \phi^m \dot{S}^m d\Omega + \int_{\Omega} \omega_m S^m \psi^m B \nabla \cdot \mathbf{v} d\Omega - \int_{\Omega} \nabla \omega_m \cdot \mathbf{q}_m d\Omega \\ = -\frac{1}{\rho_i} \int_{\Omega} \omega_m c^m d\Omega + \int_{\Gamma_{q_m}} \omega_m \hat{q}_m d\Gamma \end{aligned} \quad (44)$$

Time-Integrated Form

For the time integration of the variational equations for the mass balance, the first-order accurate, unconditionally stable backward Euler scheme is used to take advantage of its high-frequency numerical damping that suppresses spurious oscillations in time. It is noted that this feature is particularly advantageous for double-porosity problems in which the permeability contrast between the two pore scales could possibly be very significant. In other words, a time step that is acceptable for diffusion in the macropore region may not be suitable for diffusion in the micropore region, resulting in pressure oscillation with respect to time unless the backward Euler scheme is used. At time t_{n+1} , the time-integrated variational equation for the balance of mass for the macropores reads

$$\begin{aligned} \mathcal{R}_{p_M} = \int_{\Omega} \omega_M \phi^M (S^M - S_n^M) d\Omega + \int_{\Omega} \omega_M S^M \psi^M B \nabla \cdot (\mathbf{u} - \mathbf{u}_n) d\Omega \\ - \Delta t \int_{\Omega} \nabla \omega_M \cdot \mathbf{q}_M d\Omega - \frac{\Delta t}{\rho_w} \int_{\Omega} \omega_M c^M d\Omega - \Delta t \int_{\Gamma_{q_M}} \omega_M \hat{q}_M d\Gamma \\ = 0 \end{aligned} \quad (45)$$

For the micropores, the equivalent expression reads

$$\begin{aligned} \mathcal{R}_{p_m} = \int_{\Omega} \omega_m \phi^m (S^m - S_n^m) d\Omega + \int_{\Omega} \omega_m S^m \psi^m B \nabla \cdot (\mathbf{u} - \mathbf{u}_n) d\Omega \\ - \Delta t \int_{\Omega} \nabla \omega_m \cdot \mathbf{q}_m d\Omega - \frac{\Delta t}{\rho_w} \int_{\Omega} \omega_m c^m d\Omega - \Delta t \int_{\Gamma_{q_m}} \omega_m \hat{q}_m d\Gamma \\ = 0 \end{aligned} \quad (46)$$

where index n = quantities at time t_n ; and Δt = time increment. For brevity, the index $n + 1$ is omitted for terms pertaining to time t_{n+1} . Note that the residuals $\mathcal{R}_{(\cdot)}^h$ are defined after multiplying the original time-integrated equations by the time increment Δt .

Matrix Form

For spatial discretization, the standard Galerkin approximation is performed, and the displacement and two pore pressure fields are interpolated by using a three-field mixed finite element. It is worth noting that the interpolation functions for displacement and pore pressures are not arbitrary, and only a limited number of possible combinations work in practice. In the limit of fully saturated and undrained deformation, the interpolation functions must satisfy the inf-sup condition for twofold saddle point problems (Howell and Walkington 2011); otherwise, the pore pressure solution will exhibit spurious oscillations in space similar to those studied by Murad and Loula (1994) and White and Borja (2008).

With the standard shape function matrices, the trial functions are represented as

$$\left. \begin{aligned} \mathbf{u}^h &= \mathbf{N}^u \mathbf{d} + \hat{\mathbf{N}}^u \hat{\mathbf{d}} \\ p_M^h &= \mathbf{N}^p \mathbf{p}_M + \hat{\mathbf{N}}^p \hat{\mathbf{p}}_M \\ p_m^h &= \mathbf{N}^p \mathbf{p}_m + \hat{\mathbf{N}}^p \hat{\mathbf{p}}_m \end{aligned} \right\} \quad (47)$$

where superscript h = spatially discretized function; \mathbf{N} = shape function matrix, with superscript characters indicating the fields being interpolated; \mathbf{d} , \mathbf{p}_M , and \mathbf{p}_m = nodal displacement vector, nodal macropore pressure vector, and nodal micropore pressure vector, respectively; and the hats pertain to contributions from the essential boundary conditions.

The gradient and divergence of the primary variables are interpolated as follows:

$$\left. \begin{aligned} \nabla \mathbf{u}^h &= \mathbf{B} \mathbf{d} + \hat{\mathbf{B}} \hat{\mathbf{d}} \\ \nabla \cdot \mathbf{u}^h &= \mathbf{b} \mathbf{d} + \hat{\mathbf{b}} \hat{\mathbf{d}} \\ \nabla p_M^h &= \mathbf{E} \mathbf{p}_M + \hat{\mathbf{E}} \hat{\mathbf{p}}_M \\ \nabla p_m^h &= \mathbf{E} \mathbf{p}_m + \hat{\mathbf{E}} \hat{\mathbf{p}}_m \end{aligned} \right\} \quad (48)$$

The same shape functions are used for the variations, following the standard Galerkin approximation.

The matrix form of the problem is developed by inserting the finite-element approximations into the Galerkin form of the mixed variational Eqs. (42), (45), and (46). The residual equations take the vector forms as follows:

1. Balance of linear momentum

$$\begin{aligned} \mathcal{R}_u^h &= -\int_{\Omega} (\mathbf{B}^T \boldsymbol{\sigma}' - \mathbf{b}^T B \bar{p}^h) d\Omega + \int_{\Omega} (\mathbf{N}^u)^T (\rho \mathbf{g} + \bar{\mathbf{c}}) d\Omega + \int_{\Gamma_t} (\mathbf{N}^u)^T \hat{\mathbf{t}} d\Gamma \\ &\rightarrow \mathbf{0} \end{aligned} \quad (49)$$

2. Balance of mass in the macropores

$$\begin{aligned} \mathcal{R}_{p_M}^h &= \int_{\Omega} (\mathbf{N}^p)^T \phi^M (S^M - S_n^M) d\Omega + \int_{\Omega} (\mathbf{N}^p)^T S^M \psi^M B \nabla \cdot (\mathbf{u}^h - \mathbf{u}_n^h) d\Omega \\ &\quad - \Delta t \int_{\Omega} \mathbf{E} \cdot \mathbf{q}_M^h d\Omega - \frac{\Delta t}{\rho_w} \int_{\Omega} (\mathbf{N}^p)^T c^M d\Omega - \Delta t \int_{\Gamma_{q_M}} (\mathbf{N}^p)^T \hat{q}_M d\Gamma \\ &\rightarrow \mathbf{0} \end{aligned} \quad (50)$$

3. Balance of mass in the micropores

$$\begin{aligned} \mathcal{R}_{p_m}^h &= \int_{\Omega} (\mathbf{N}^p)^T \phi^m (S^m - S_n^m) d\Omega + \int_{\Omega} (\mathbf{N}^p)^T S^m \psi^m B \nabla \cdot (\mathbf{u}^h - \mathbf{u}_n^h) d\Omega \\ &\quad - \Delta t \int_{\Omega} \mathbf{E} \cdot \mathbf{q}_m^h d\Omega - \frac{\Delta t}{\rho_w} \int_{\Omega} (\mathbf{N}^p)^T c^m d\Omega - \Delta t \int_{\Gamma_{q_m}} (\mathbf{N}^p)^T \hat{q}_m d\Gamma \\ &\rightarrow \mathbf{0} \end{aligned} \quad (51)$$

Here, the equalities to zero in the previous variational equations are replaced with rightward arrows tending to zero to imply that a Newton-Raphson iteration scheme may be involved in driving the residual vectors, $\mathcal{R}_{(\cdot)}^h$, to zero (for nonlinear problems).

The previously defined residuals are generally nonlinear with respect to the primary variables \mathbf{d} , \mathbf{p}_M , and \mathbf{p}_m due to material and/or geometric nonlinearities. A Newton-Raphson iteration is thus used to solve the problem. The linearized problem is defined by a tangent operator (or Jacobian matrix) with a 3×3 block structure of the form

$$\begin{bmatrix} A & B_1 & C_1 \\ B_2 & D & E_1 \\ C_2 & E_2 & F \end{bmatrix} \begin{Bmatrix} \delta \mathbf{d} \\ \delta \mathbf{p}_M \\ \delta \mathbf{p}_m \end{Bmatrix} = - \begin{Bmatrix} \mathcal{R}_u^h \\ \mathcal{R}_{p_M}^h \\ \mathcal{R}_{p_m}^h \end{Bmatrix} \quad (52)$$

where $\delta \mathbf{d}$, $\delta \mathbf{p}_M$, and $\delta \mathbf{p}_m$ = relevant search directions. The individual submatrices of the tangent operator are given in the Appendix. Note that the tangent operator is generally nonsymmetric.

Numerous strategies for the solution of the linearized system are available. Direct methods for nonsymmetric matrices could be used, but for large systems, they could be prohibitively expensive because of the time-consuming factorization step and large memory requirements involved in the calculations. Here, an iterative solver based on the Krylov subspace methods is used. To make use of this iterative solver, the block-preconditioning technique proposed by White and Borja (2011) has been extended to accommodate the 3×3 block-partitioned structure of the tangent operator.

Numerical Examples

This section presents two numerical examples that demonstrate the impact of double porosity on the ensuing hydromechanical responses of geotechnical structures. The examples compare the structural responses predicted by double-porosity simulations with those obtained by equivalent homogenized single-porosity simulations. The first example involves the development of a persistent shear band in a laboratory-scale plane-strain compression of an aggregated soil with imposed heterogeneity in the pore fractions. The second example deals with the impact of double porosity on fluid flow and deformation of a field-scale unsaturated slope subjected to rainfall infiltration.

All computations were conducted by using Geocentric, a massively parallel finite-element code for geomechanics that is built on the deal.II finite-element library (Bangerth et al. 2007, 2013), p4est mesh handling library (Burstedde et al. 2011), and the Trilinos project (Heroux and Willenbring 2012). The implementation of this code has been verified by checking to see that, when either one of the two pore fractions is reduced to zero, the results of double-porosity simulations are identical to the results of single-porosity simulations (Borja 2004; Borja and White 2010a). It was confirmed first-hand that the problems at hand are not subject to the inf-sup stability condition because compressible air is present throughout the simulations. The results presented in the following section were obtained by equal-order linear interpolations of the displacement and two pressure variables.

Persistent Shear Band

The first example involves a rectangular specimen of an aggregated soil with a uniform overall porosity and subjected to plane-strain compression. The flow condition is locally drained but globally undrained (i.e., water cannot flow through the exterior boundaries,

but is otherwise free to migrate within the specimen). Air pressure is assumed to remain at zero within the specimen. The top and bottom boundaries of the specimen are free to slide horizontally, whereas the two vertical boundaries are subjected to a uniform external pressure. Under this condition, a single-porosity formulation would predict that stresses, pore water pressures, and deformations would be uniformly distributed throughout the specimen. No persistent shear band would form, and at the bifurcation point, two conjugate shear bands could possibly form through any point within the specimen. In other words, from a modeling standpoint, the specimen may be considered an element and not a structure.

Previous studies reveal that imperfections in the form of quantified heterogeneity can trigger a persistent shear band in unsaturated porous materials. Two types of heterogeneity have been considered in the past: one arising from nonuniform density and another emanating from an inhomogeneous degree of saturation (Andrade and Borja 2006, 2007; Borja and Andrade 2006; Borja et al. 2013a, b; Song and Borja 2014a, b). This example investigates a third form of heterogeneity that is unique to double-porosity formulation: a spatially varying pore (or void) fraction. The following simulations consider an unsaturated porous material with uniform overall density and uniform global degree of saturation, but with a spatially varying pore fraction.

A rectangular specimen 0.05 m wide and 0.10 m tall with a uniformly distributed total porosity of 0.4 was modeled with 1,040 quadrilateral mixed elements. The following material parameters were assumed in the simulations: intrinsic permeabilities, $k_M = 2 \times 10^{-10} \text{ m}^2$ and $k_m = 1 \times 10^{-13} \text{ m}^2$; dynamic viscosity of water, $\mu_w = 10^{-6} \text{ kPa} \cdot \text{s}$; diffusive mass exchange parameters, $\bar{k} = 10^{-4} \times \min(k_{rM}k_M, k_{rm}k_m)$, $a = 10^{-3} \text{ m}$, $\beta = 4$, and $\gamma = 0.4$ for Eq. (23), which are somewhat similar to the parameters used by Gerke and van Genuchten (1993a). For the water retention curves, the van Genuchten model was used for the two pore scales, with $S_1^M = 0.1$, $S_2^M = 1.0$, $n_M = 4$, and $s_{\alpha M} = 2.5 \text{ kPa}$ for the macropores and $S_1^m = 0.2$, $S_2^m = 1.0$, $n_m = 2$, and $s_{\alpha m} = 25 \text{ kPa}$ for the micropores. This difference in the water retention parameters was motivated by the fact that the macropores typically have a smaller air-entry value than the micropores (Romero et al. 1999, 2011).

For the solid matrix, a non-associative Drucker-Prager plasticity model was used, with a friction angle of $\phi = 30^\circ$ and dilation angle of $\psi = 5^\circ$. Cohesion of aggregated soils can be significantly high (Fuentes et al. 2013), but it may quickly decrease when aggregated structures degrade by plastic strain. This aspect was considered by assuming an initial cohesion of 15 kPa and adopting a cohesion softening law presented by Borja (2013), which is given by

$$c = c_0 \exp[-(\lambda/k_1)^2] \quad (53)$$

where c and c_0 = current and initial cohesion; k_1 = positive constant; and λ = cumulative plastic strain defined as

$$\lambda = \int_t \|\dot{\epsilon}^p\| \, dt \quad (54)$$

where ϵ^p = plastic part of the infinitesimal strain tensor. This softening law was used with $k_1 = 0.01$. For the numerical integration of this plasticity model, the readers are referred to Chapter 4 of Borja (2013). Note that, although the yield surface does not explicitly take the suction stress as a parameter, the plastic response does depend on the suction because it is incorporated into the definition of the effective stress. Isotropic linear elasticity was assumed inside the yield surface, with elastic bulk modulus $K = 5 \text{ MPa}$ and Poisson's ratio $\nu = 0.3$. The solid grains were assumed to be incompressible,

resulting in a Biot coefficient of $B = 1$. The gravity load was neglected in the simulations.

The soil was initially unsaturated with a uniform suction of 5 kPa in the macropores and micropores, resulting in a uniformly distributed global degree of saturation of 0.58. Two macroporosity distributions were generated statistically by using a normal distribution function with a specified mean of 0.2 and a standard deviation of 0.01. Two realizations, labeled Case #1 and Case #2 and having macropore fractions ranging from a low value of 0.41 to a high value of 0.59, are shown in Fig. 2. Because of the significant difference in the water retention characteristics, the initial local saturations in the two pore regions were nearly at the extreme ends of the spectrum (0.11 for the macropores and 0.98 for the micropores), which means that most of the pore water was initially inside the micropores. After the initial conditions were established, the specimen was consolidated by an isotropic pressure of 100 kPa and then compressed by the top boundary moving downward by 2×10^{-5} m

for each time increment. Note that, whereas the mechanical model is rate independent, the overall hydromechanical response is rate dependent because of the presence of fluid flow.

Fig. 3 portrays the equivalent plastic strain $\sqrt{2/3}\lambda$ for the two cases at a vertical compression of 2.7 mm. Note that for each of the two initial macropore fraction distributions, a unique shear band develops (one is the conjugate of the other) and that the locations of the two persistent shear bands are uniquely identified. The orientations of the two shear bands are approximately $47\text{--}48^\circ$ from horizontal, which is fairly close to the Roscoe angle of $45^\circ + \psi/2$. This result indicates that heterogeneity in the pore fractions can also be an effective trigger of a shear band and, more specifically, a persistent shear band that has unique orientation and position in an otherwise homogeneously deforming body. It is clear that this result cannot be generated from a modeling framework that relies solely on single-porosity formulation, which is not capable of distinguishing between the properties of the macropore and micropore regions.

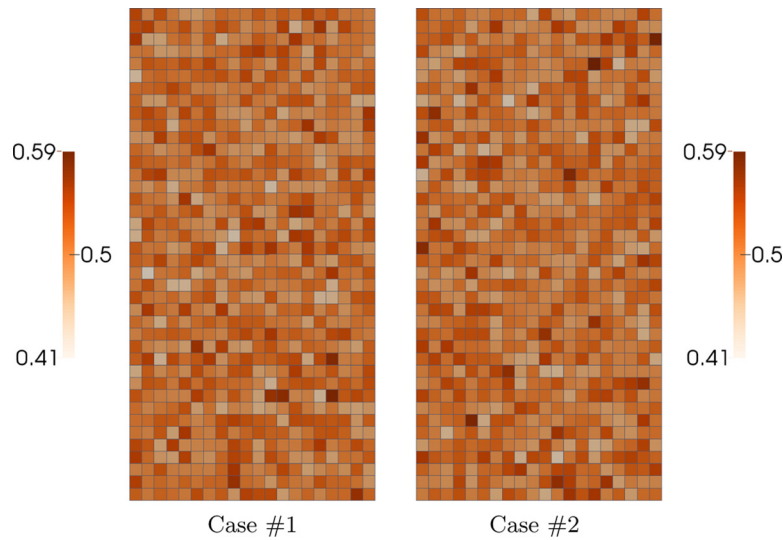


Fig. 2. Spatial distributions of macropore fractions, ψ^M ; note that the overall porosities of the two distributions are the same and are uniformly distributed throughout the specimen

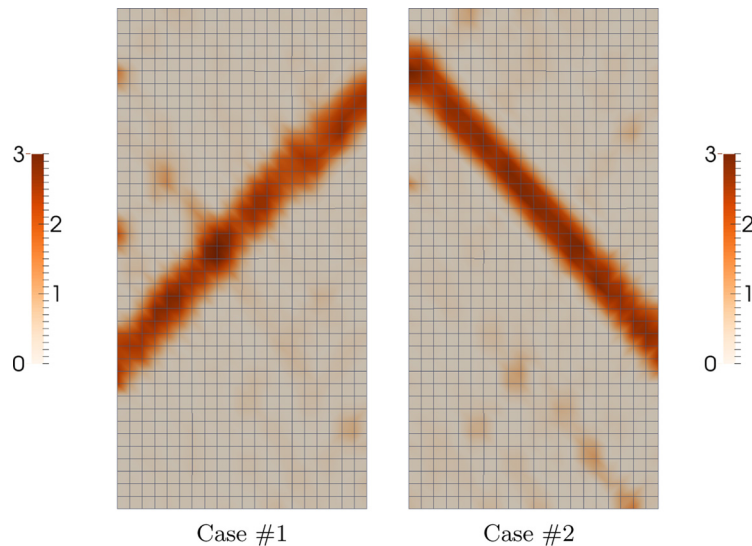


Fig. 3. Contours of equivalent plastic strain (percentage) at vertical compression of 2.7 mm

Fig. 4 shows contours of the mean pore pressure (\bar{p}) at the same vertical compression of 2.7 mm. Note that \bar{p} , which accommodates both the macropore and micropore water pressures, is positive everywhere, although lower values are detected in the zone of the persistent shear band due to greater plastic dilatancy predicted by the Drucker-Prager model in this region. However, this result does not imply that both the macropore and micropore pressures are positive inside the specimen. In fact, Fig. 5 shows that the macropore water pressures barely changed from their initial value of -5 kPa, but the micropore water pressures dramatically increased as a result of the imposed specimen deformation (induced primarily by the very low permeability of the micropores). Because the mean pore pressure (\bar{p}) is calculated from the two pressures weighted according to their pore fractions and local degrees of saturation, and because the micropore water pressures are well above zero, the resulting overall pore pressures inside the specimen are positive for both cases.

An interesting consequence of the fact that the macropore water pressures barely changed from their initial negative values is that the macropores remain essentially unsaturated even as the micropores reach full saturation. Fig. 6 affirms this statement: the degrees of saturation in the macropores barely increased from their initial value of 0.11, even as the micropores reached full saturation for both cases. Because the global degree of saturation is the weighted average of the individual degrees of saturation, the specimen as a whole remains unsaturated even as the mean pore pressure is positive. Of course, a positive overall pressure on an unsaturated porous medium cannot be explained in the context of single porosity formulation—only by treating the two pore regions explicitly can one explain how this unique combination of hydrologic states can occur. On a related note, an approach often used to reconcile the aforementioned unique combination in the context of single-porosity formulation is to ignore suctions in the macropores and simply take the

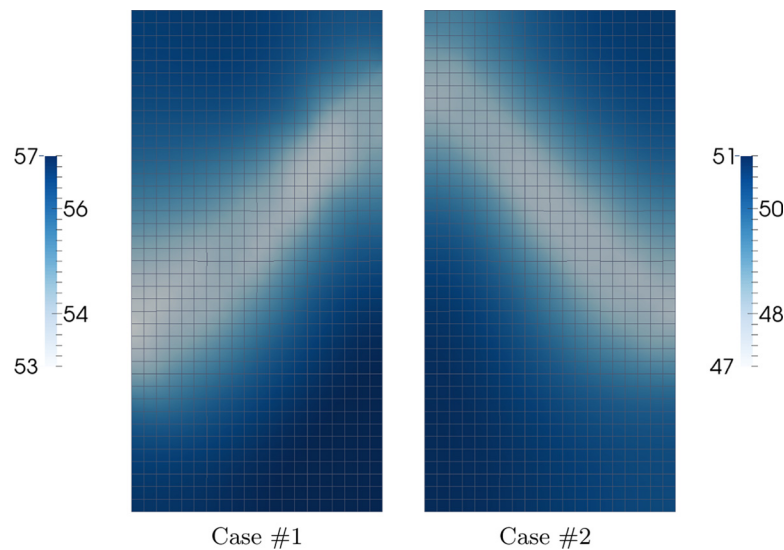


Fig. 4. Contours of mean pore water pressure, \bar{p} (in kPa), for Cases #1 and #2 calculated at vertical compression of 2.7 mm

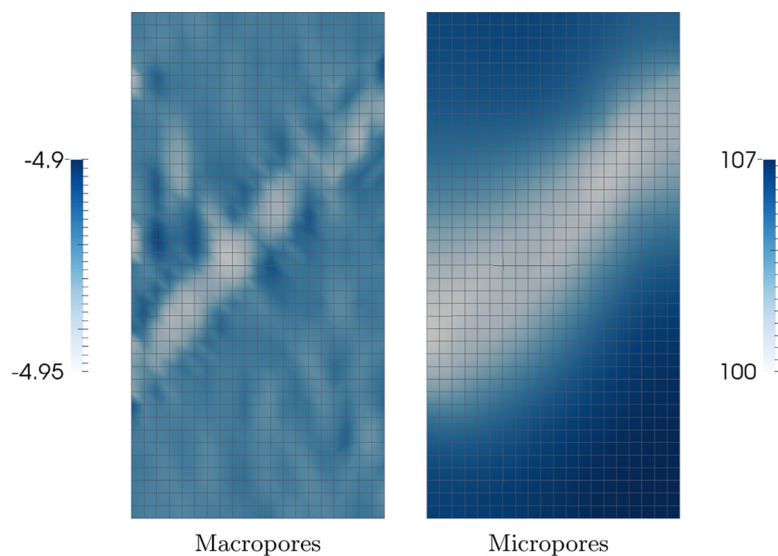


Fig. 5. Contours of macropore and micropore water pressures (in kPa) for Case #1 calculated at vertical compression of 2.7 mm

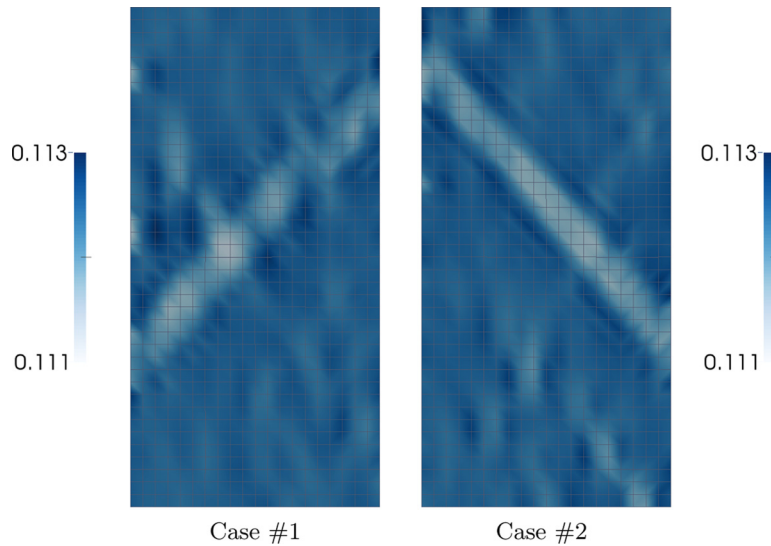


Fig. 6. Contours of degree of saturation for the macropores at vertical compression of 2.7 mm; note that the micropores are fully saturated everywhere at this loading stage

microsaturation as the global saturation (Koliji et al. 2010a). However, this may be an oversimplification for materials that can have non-trivial suctions in the macropores, such as those studied by Romero et al. (1999, 2011).

Unsaturated Slope under Rainfall Infiltration

The second example involves a steep hillside slope subjected to rainfall infiltration. The problem is similar to the one simulated by Borja and White (2010b) and Borja et al. (2012b, a): a steep slope made up of a thin layer of colluvium approximately 1–2 m thick and underlain by a rigid but highly fractured bedrock was subjected to rainfall infiltration. Rainfall was applied on the surface of the slope in the form of a flux that infiltrated into the colluvium, saturating it and causing the slope to form localized plastic shear zones. Different drainage conditions into the bedrock were investigated in the previous works (Borja and White 2010b; Borja et al. 2012b, a), and here, for simplicity, the bedrock was assumed to be impermeable. To investigate the impact of multiscale properties of the colluvium, this example assumed the colluvium to be a double-porosity medium and compared the ensuing hydromechanical response with that obtained from a single-porosity medium with the same overall material properties.

Single-Porosity Modeling

The colluvium was first considered as a single-porosity material. Fig. 7 portrays the geometry and finite-element mesh for the slope, modeled in this example as a plane-strain problem. The colluvium domain was discretized with 649 quadrilateral mixed elements, and its bottom layer was fixed to the bedrock, which was assumed to be rigid and impermeable. This boundary condition means that sliding of the colluvium could only take place in the form of plastic bulk shearing of elements attached to the bedrock. The top and bottom vertical boundaries of the colluvium are no-flow boundaries (i.e., impervious walls). These boundary constraints could impact the flow patterns during advanced periods of sustained rainfall, as elaborated later.

Intrinsic mass densities of $\rho_s = 2.6 \text{ t/m}^3$ were assumed for the solid grains and $\rho_w = 1.0 \text{ t/m}^3$ for water. The porosity of the solid matrix was 0.39, which is similar to that of the aggregated soil tested by Carminati et al. (2007). For the mechanical modeling, a

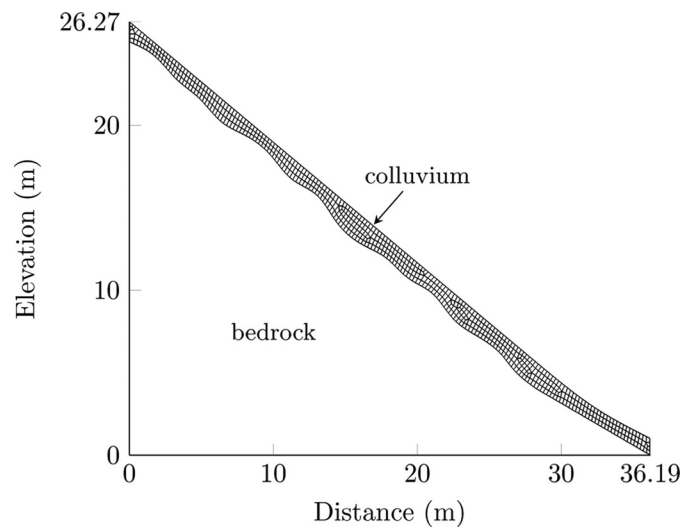


Fig. 7. Geometry and mesh for the steep hillside slope problem

thermodynamically consistent effective stress tensor derived by Borja (2006) was used. A Biot coefficient of $B = 1$ was assumed, which is reasonable for soils. An elastic–perfectly plastic Drucker–Prager model was used with the following parameters: bulk modulus $K = 10 \text{ MPa}$, Poisson’s ratio $\nu = 0.35$, cohesion $c = 2.5 \text{ kPa}$ (derived primarily from plant roots), friction angle $\phi = 38^\circ$, and dilation angle $\psi = 25^\circ$. These parameters are similar to those used in previous simulations conducted by the authors (Borja and White 2010b; Borja et al. 2012a, b).

For the water retention model, a van Genuchten curve was fitted to the experimental data for an aggregated soil presented by Carminati et al. (2007). Reference data obtained for an assembly of aggregates in which pore water was retained in both the inter-aggregate and intra-aggregate pores were used to determine the homogenized properties for an equivalent single-porosity material. The following parameters were obtained for the equivalent single-porosity material: residual saturation $S_1 = 0.2$, maximum saturation $S_2 = 1.0$, shape parameter $n = 1.92$, and scaling suction $s_\alpha = 25 \text{ kPa}$. For fluid diffusion, an intrinsic permeability of $k = 10^{-11} \text{ m}^2$ and a dynamic viscosity of

water of $\mu_w = 10^{-6}$ kPa · s were assigned. An initial uniform suction of 25 kPa was assumed throughout the slope.

The initialization phase consisted of applying static gravity load to the colluvium to establish the initial stress conditions at the quadrature points and then resetting the nodal displacements to zero. Then, rainfall was simulated by applying a normal water flux of $\hat{q} = 50$ mm/h on the slope surface, a natural boundary condition in the

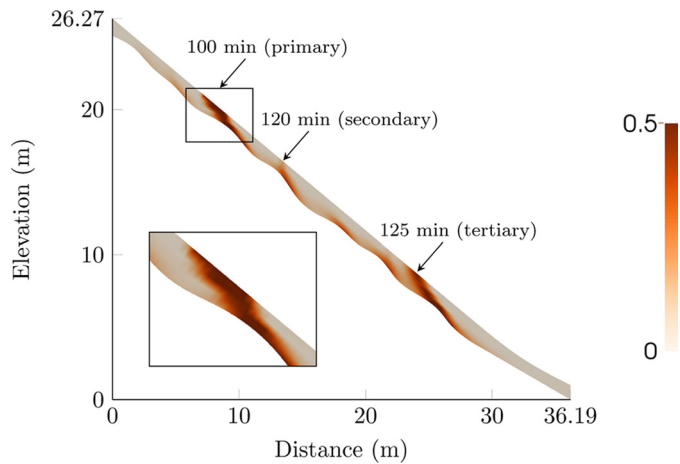


Fig. 8. Single porosity: equivalent plastic strain (percentage) in the colluvium at $t = 125$ min

terminology of the finite-element method. An important consideration in rainfall infiltration simulation is that the pore water pressure cannot be greater than zero on the slope face. To ensure that this flow physics is satisfied, any exfiltration of water from the slope face was monitored, and once a positive pore pressure was detected on the slope face, the boundary condition was switched to zero pressure, an essential boundary condition. The fluid flux was applied until the slope developed localized deformation patterns.

Fig. 8 shows a snapshot of plastic strains that developed within the slope after 125 min of rainfall. The slope exhibited a multiple block failure mechanism analogous to the results reported by Borja and White (2010b) and Borja et al. (2012b) and explained further by Varnes (1978). Development of zones of localized deformation took place progressively. After 100 min of rainfall, a localized zone emerged on the slope face (primary), followed by another zone at 120 min (secondary) and then a third zone at 125 min (tertiary). Note that deformation in the tertiary zone was more intense than deformation that developed in the secondary zone. As the tertiary zone of localized deformation developed, the global Newton-Raphson iteration showed a much slower (sublinear) convergence rate. Such behavior of the iterative solution is quite common and is often interpreted as a sign of an impending slope failure, although such inference is not made in this work. It is noted that a similar sublinear convergence rate was observed as the persistent shear band developed progressively in the rectangular specimen of the previous example.

Fig. 9 shows contours of degree of saturation and pore water pressure in the colluvium after 100 min of rainfall, which is the

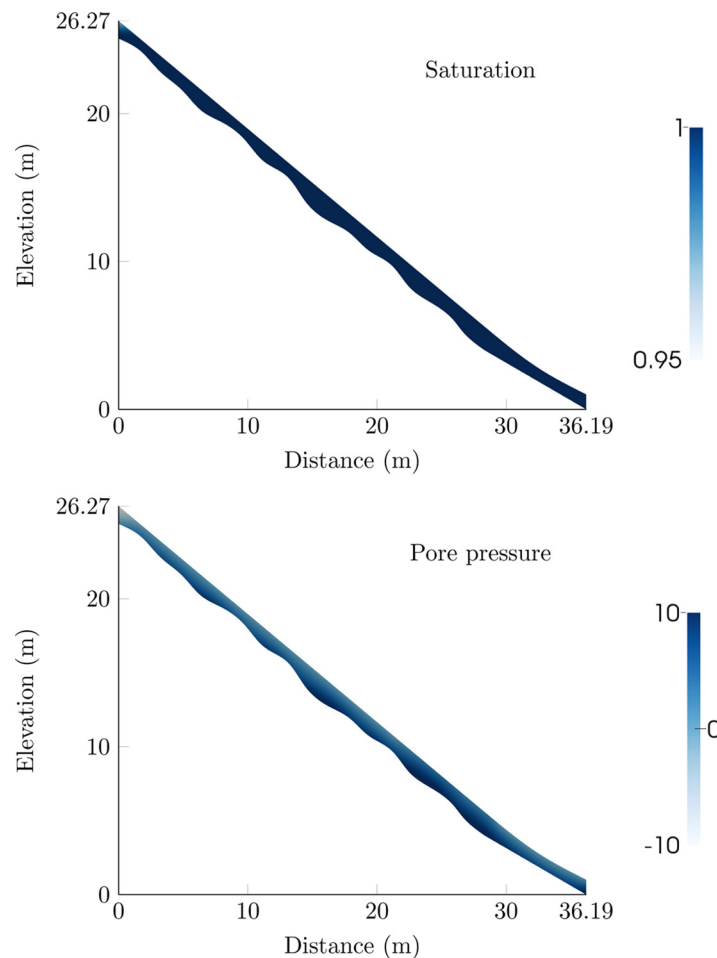


Fig. 9. Single porosity: degree of saturation and pore water pressure (in kPa) in the colluvium at $t = 100$ min

time instant at which the primary plastic zone emerged on the slope face. It is clear that the location of the intense plastic zone correlates well with the zone of full saturation in which the pore water pressures increased to a value greater than zero, which implies that loss of suction was the primary reason for the development of the localized plastic zone. On the other hand, Fig. 10 depicts the degree of saturation and pore water pressure after 125 min of rainfall. At that time instant, the entire colluvium domain was nearly fully saturated, which resulted in the development of the secondary and tertiary plastic zones.

It is noted that the zone of full saturation in the colluvium domain developed from both the top and bottom end boundaries of the mesh and converged somewhere in the middle of the slope. It is obvious that the vertical wall at the bottom end of the mesh blocked fluid flow, which caused the saturated zone to propagate uphill under the sustained rainfall. However, the vertical wall at the top end of the mesh did not affect the development of a saturated zone that propagated downhill; rather, it is the combined effects of rainfall intensity, colluvium geometry, and permeability that were responsible for saturating the top end of the mesh. These flow dynamics are revisited in the context of double-porosity simulation in the next section.

Double-Porosity Modeling

The next step of the analysis entails converting the colluvium domain into a double-porosity medium. To have a meaningful comparison with the single-porosity simulation, the overall porosity of the double-porosity medium must be the same as that

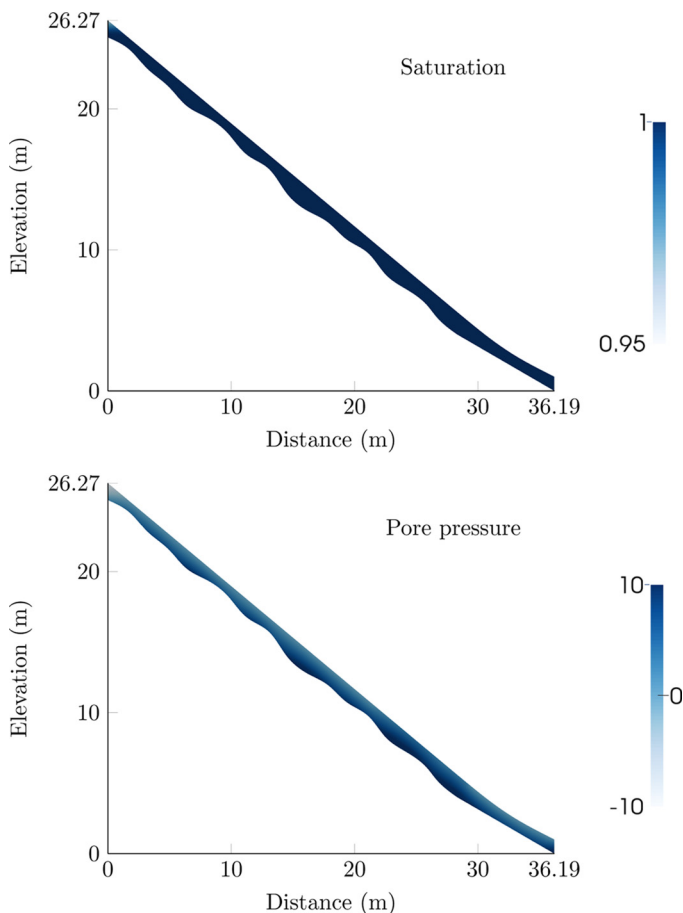


Fig. 10. Single porosity: degree of saturation and pore water pressure (in kPa) in the colluvium at $t = 125$ min

of the single-porosity medium, which means that the total porosity of the double-porosity medium must somehow be distributed to the two pore scales. Here 0.09 of the porosity was arbitrarily assigned to the macropores and 0.3 of it to the micropores, for a total porosity of 0.39. The next step was to assign water retention characteristics to the two pore scales such that the overall water retention characteristics were comparable to those of the single-porosity medium. To this end, the experimental data reported by Carminati et al. (2007) were used as a reference, and their data were calibrated by superimposing water retention curves for the two pore scales. This calibration entails a trial-and-error procedure, and the results are shown in Fig. 11. In this figure, the two dashed curves are the water retention curves for the two pore scales; the red curve is the superposition of the two dashed curves, and the blue curve is the water retention curve used in the single-porosity simulation.

The superposition of the two water retention curves was based on the definition of global degree of saturation for a double-porosity medium, as seen in Eq. (8). Here, the fact that the air-entry value for the micropores is typically much higher than that for the macropores was used. A similar superposition approach was used in the literature (Durner 1994; Buscarnera and Einav 2012; Casini et al. 2012). The calibration described in the preceding paragraph yielded the following van Genuchten parameters. For the macropores, $S_1^M = 0.05$, $S_2^M = 1.0$, $n_M = 3$, and $s_{aM} = 12$ kPa; for the micropores, $S_1^m = 0.2$, $S_2^m = 1.0$, $n_m = 2.2$, and $s_{cm} = 50$ kPa. The corresponding permeabilities for the macropores and micropores are 4.33×10^{-11} and 4.33×10^{-15} m², respectively.

The mechanical properties used for the solid component were the same as those used in the single-porosity simulation. Note that, whereas the elastoplastic parameters were the same as in the previous case, the total suction was obtained from the combination of the local macropore and micropore suctions. Last, the following values were assumed for the diffusive mass transfer: $a = 0.01$ m, $\beta = 11$, $\gamma = 0.4$, and $\bar{k} = 0.01 \times \min(k_{rM}k_M, k_{rm}k_m)$.

Simulations were conducted in exactly the same manner as in the single-porosity case. The same initial suction of 25 kPa was specified at the two pore scales so that the initial stress condition of the slope remained the same and pore water pressures were in local equilibrium. As in the previous example, the macropores were much drier than the micropores under the same suction because of their water retention characteristics.

Care must be taken to ensure a realistic modeling of the flux boundary condition. Here, the rainfall was allowed to infiltrate the macropores only, not the micropores, because of the very low

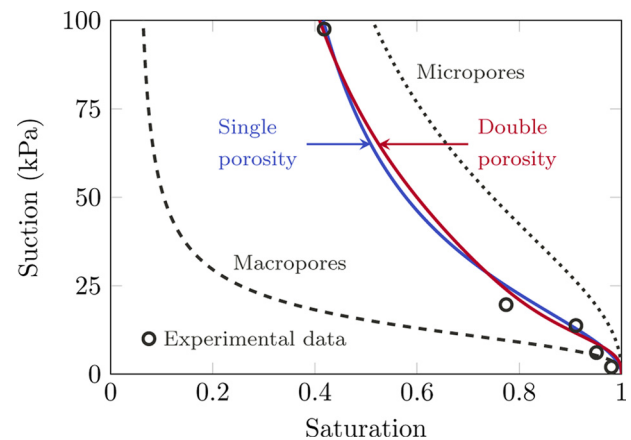


Fig. 11. Water retention curves for double-porosity and single-porosity modeling fitted to experimental data from Carminati et al. (2007)

permeability of the micropores. In other words, the flux boundary condition was set to zero for the micropores, but it was set equal to the full rainfall intensity value of $\hat{q} = 50$ mm/h for the macropores. This assumed that the macropores were permeable enough to accommodate all of the rainfall volume without surface runoff.

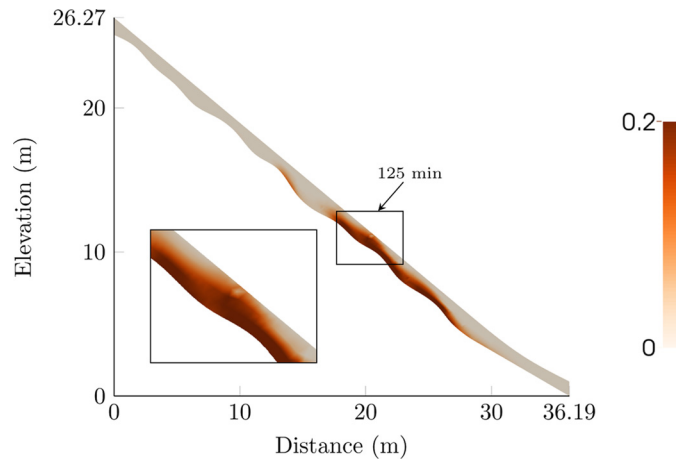


Fig. 12. Double porosity: equivalent plastic strain (percentage) in the colluvium at $t = 125$ min

These flow conditions are similar to those used in the numerical experiments conducted by Gerke and van Genuchten (1993a).

The failure pattern in the slope predicted by the double-porosity simulation was investigated first. Fig. 12 shows the contour of plastic strain after 125 min of rainfall. It was observed that the simulation predicted only one zone of intense deformation, unlike the single-porosity simulation, which predicted three localized yield zones. This plastic zone was located between the secondary and tertiary zones of the single-porosity simulation. The fact that this zone of intense deformation emerged at almost the same time instant as the moment at which the single-porosity simulation developed a tertiary localized zone may be attributed to the fact that the colluvium was made to accommodate approximately the same volume of rainwater that saturated the lower end of the mesh. However, there was no primary or secondary localized shear zone predicted by the double-porosity simulation.

To explain the difference between the mechanisms of deformation predicted by the single and double-porosity simulations, the contours of overall degree of saturation and mean pore water pressure at time instants $t = 100$ and 125 min are plotted in Figs. 13 and 14, respectively, and compared with those calculated from the single-porosity simulations portrayed in Figs. 9 and 10, respectively. Recall that the mean pore water pressure (\bar{p}) determines the effective stress, which in turn determines the plastic yield zone. Fig. 13 shows that, at $t = 100$ min, the colluvium domain remained unsaturated for the most

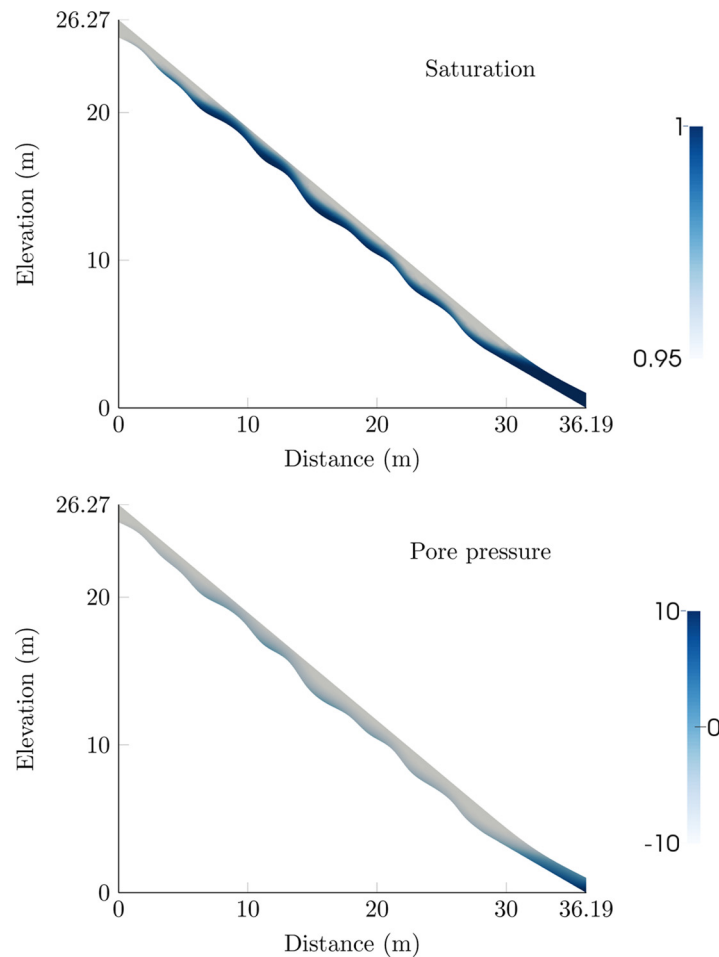


Fig. 13. Double porosity: global degree of saturation and mean pore water pressure (in kPa) in the colluvium at $t = 100$ min

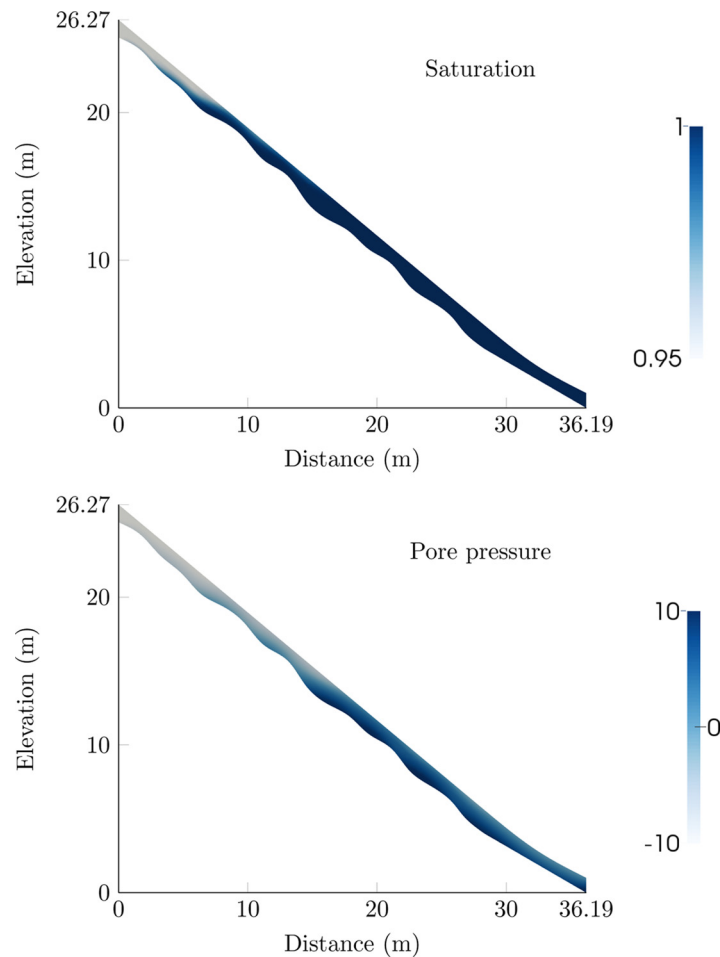


Fig. 14. Double porosity: global degree of saturation and mean pore water pressure (in kPa) in the colluvium at $t = 125$ min

part, except near the soil-bedrock interface, which reached full saturation. This result could be attributed to the much higher permeability of the macropores that allowed the rainwater to flow more freely underneath the slope. In contrast, the permeability of the single-porosity medium was not high enough to allow the rainwater to flow as freely, and so a bottleneck formed that caused the upper segment of the slope to become fully saturated. This result leads to the important conclusion that, in a double-porosity medium, it is the permeability of the macropores, and not the average permeability, that determines the resulting flow pattern.

The difference in deformation and flow patterns in a double-porosity formulation may be attributed to the preferential/non-equilibrium flow. Indeed, this is a major feature that distinguishes double-porosity flow from single-porosity flow (Šimůnek et al. 2003; Gerke 2006; Jarvis 2007). The occurrence of non-equilibrium flow can be examined by checking whether the macropore and micropore pressures are different at the same local point. Fig. 15 shows the pressure difference ($p_M - p_m$) in the slope at four time instants. The figure confirms that local non-equilibrium existed throughout the entire rainfall period, suggesting that the flow physics was different from that of the single-porosity case. This difference impacted the evolution of pressure/saturation and resulted in a different failure mechanism. It also highlights the fact that an equivalent single-porosity modeling of a double-porosity material may not be justified in the context of a boundary value problem. In other

words, conversion of a double-porosity medium into an equivalent single-porosity medium is a gross simplification, and the approach could generate misleading results when applied to boundary value problems.

Closure

This paper has presented a hydromechanical framework for unsaturated porous media with two dominant pore scales. The framework relies on a thermodynamically consistent definition of effective stress, a measure of stress that is energy-conjugate to the rate of deformation of the solid matrix. The same thermodynamic framework has enabled identification of other state variables that must be linked via constitutive laws, including the transfer of fluid mass between the two pore scales that must be related via a constitutive law to the difference in pore pressures at the two scales. A mixed finite-element formulation was used to solve boundary value problems for unsaturated porous media with double porosity.

In previous papers, it has been shown that heterogeneity in density and degree of saturation can have a first-order effect on the development of a persistent shear band in porous materials. The work presented in this paper has shown that a third form of heterogeneity, emanating from the spatial distribution of the pore fraction, can also have a significant impact on the

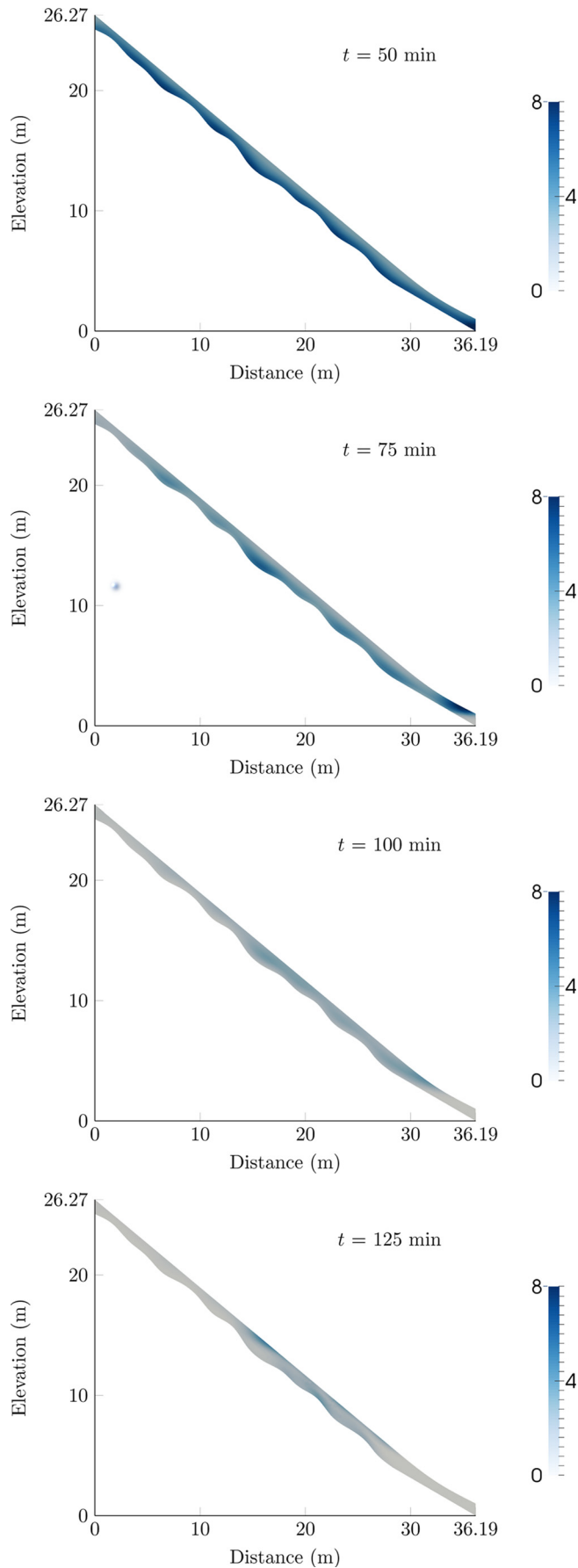


Fig. 15. Snapshots of pressure differences (in kPa) between the macropores and micropores during the rainfall

development of a persistent shear band. Two numerical examples have been used to demonstrate the impact of double porosity on the deformation and flow patterns. The first example demonstrates a unique condition that is not possible with single-porosity theory: an unsaturated mixture of solid, water, and air with an overall positive pore water pressure. The second example suggests that failure mechanisms in slopes can be significantly altered by an explicit treatment of the two pore scales. Although the results from the first example may be intuitive, the results from the second example are more quantitative in the sense that the new failure patterns can be captured only by a robust computational model that accounts for the two pore scales.

Acknowledgments

This material is based on work supported by the U.S. Department of Energy, Office of Science, Office of Basic Energy Sciences, Geosciences Research Program, under Award Number DE-FG02-03ER15454. Financial support for the first author was provided by the Fulbright Program and the John A. Blume Earthquake Engineering Center.

Appendix. Submatrices of the Tangent Operator

The submatrices of the tangent operator in Eq. (52) are given by

$$A = - \int_{\Omega} \mathbf{B}^T \mathbf{C}_k \mathbf{B} d\Omega \quad (55)$$

$$B_1 = \int_{\Omega} \left[\mathbf{b}^T B \left(S^M \psi^M + \frac{\partial S^M}{\partial p_M^h} p_M^h \right) + (\mathbf{N}^u)^T \left(\frac{\partial \rho}{\partial p_M^h} \mathbf{g} + \frac{\partial \bar{c}^h}{\partial p_M^h} \right) \right] \mathbf{N}^p d\Omega \quad (56)$$

$$C_1 = \int_{\Omega} \left[\mathbf{b}^T B \left(S^m \psi^m + \frac{\partial S^m}{\partial p_m^h} p_m^h \right) + (\mathbf{N}^u)^T \left(\frac{\partial \rho}{\partial p_m^h} \mathbf{g} + \frac{\partial \bar{c}^h}{\partial p_m^h} \right) \right] \mathbf{N}^p d\Omega \quad (57)$$

$$B_2 = \int_{\Omega} (\mathbf{N}^p)^T B S^M \psi^M \mathbf{b} d\Omega \quad (58)$$

$$D = \int_{\Omega} (\mathbf{N}^p)^T \frac{\partial S^M}{\partial p_M^h} [\phi^M + \psi^M B \nabla \cdot (\mathbf{u}^h - \mathbf{u}_n^h)] \mathbf{N}^p d\Omega + \Delta t \int_{\Omega} \mathbf{E}^T \left[\boldsymbol{\kappa}_M \mathbf{E} + \frac{\partial \boldsymbol{\kappa}_M}{\partial p_M^h} (\nabla p_M^h - \rho_w \mathbf{g}) \right] \mathbf{N}^p d\Omega \quad (59)$$

$$- \frac{\Delta t}{\rho_w} \int_{\Omega} (\mathbf{N}^p)^T \left(\frac{\partial c^M}{\partial p_M^h} \right) \mathbf{N}^p d\Omega$$

$$E_1 = - \frac{\Delta t}{\rho_w} \int_{\Omega} (\mathbf{N}^p)^T \left(\frac{\partial c^M}{\partial p_M^h} \right) \mathbf{N}^p d\Omega \quad (60)$$

$$C_2 = \int_{\Omega} (\mathbf{N}^p)^T B S^m \psi^m \mathbf{b} d\Omega \quad (61)$$

$$E_2 = - \frac{\Delta t}{\rho_w} \int_{\Omega} (\mathbf{N}^p)^T \left(\frac{\partial c^m}{\partial p_m^h} \right) \mathbf{N}^p d\Omega \quad (62)$$

$$\begin{aligned}
F = & \int_{\Omega} (\mathbf{N}^p)^T \frac{\partial S^m}{\partial p_m^h} [\phi^m + \psi^m B \nabla \cdot (\mathbf{u}^h - \mathbf{u}_n^h)] \mathbf{N}^p d\Omega \\
& + \Delta t \int_{\Omega} \mathbf{E}^T \left[\boldsymbol{\kappa}_m \mathbf{E} + \frac{\partial \boldsymbol{\kappa}_m}{\partial p_m^h} (\nabla p_m^h - \rho_w \mathbf{g}) \mathbf{N}^p \right] d\Omega \\
& - \frac{\Delta t}{\rho_w} \int_{\Omega} (\mathbf{N}^p)^T \left(\frac{\partial c^m}{\partial p_m^h} \right) \mathbf{N}^p d\Omega \quad (63)
\end{aligned}$$

where \mathbf{C}_k = consistent stress-strain matrix (k denotes an iteration counter); and $\boldsymbol{\kappa}_{(\cdot)}$ = matrix of permeability coefficients $k_{r(\cdot)}k_{(\cdot)}/\mu_w$.

References

- Abousleiman, Y. N., Hoang, S. K., and Liu, C. (2014). "Anisotropic poro-thermoelastic solution and hydro-thermal effects on fracture width in hydraulic fracturing." *Int. J. Numer. Anal. Methods Geomech.*, 38(5), 493–517.
- Andrade, J. E., and Borja, R. I. (2006). "Capturing strain localization in dense sands with random density." *Int. J. Numer. Methods Eng.*, 67(11), 1531–1564.
- Andrade, J. E., and Borja, R. I. (2007). "Modeling deformation banding in dense and loose fluid-saturated sands." *Finite Elem. Anal. Des.*, 43(5), 361–383.
- Bangerth, W., Hartmann, R., and Kanschä, G. (2007). "deal. II: A general-purpose object-oriented finite element library." *ACM Trans. Math. Software*, 33(4).
- Bangerth, W., et al. (2013). "The deal. II Library, Version 8.1." arXiv preprint, 1312.2266.
- Barenblatt, G., Zheltov, Iu, P., and Kochina, I. N. (1960). "Basic concepts in the theory of seepage of homogeneous liquids in fissured rocks." *J. Appl. Math. Mech.*, 24(5), 1286–1303.
- Bennett, K. C., Berla, L. A., Nix, W. D., and Borja, R. I. (2015). "Instrumented nanoindentation and 3D mechanistic modeling of a shale at multiple scales." *Acta Geotech.*, 10(1), 1–14.
- Berkowitz, B., Bear, J., and Braester, C. (1988). "Continuum models for contaminant transport in fractured porous formations." *Water Resour. Res.*, 24(8), 1225–1236.
- Borja, R. I. (2004). "Cam-clay plasticity. Part V: A mathematical framework for three-phase deformation and strain localization analyses of partially saturated porous media." *Comput. Methods Appl. Mech. Eng.*, 193(48–51), 5301–5338.
- Borja, R. I. (2006). "On the mechanical energy and effective stress in saturated and unsaturated porous continua." *Int. J. Solids Struct.*, 43(6), 1764–1786.
- Borja, R. I. (2013). *Plasticity: Modeling and computation*. Springer-Berlin.
- Borja, R. I. (2014). *Computational poromechanics. Lecture Notes*. Stanford University, Stanford, CA.
- Borja, R. I., and Andrade, J. E. (2006). "Critical state plasticity. Part VI: Meso-scale finite element simulation of strain localization in discrete granular materials." *Comput. Methods Appl. Mech. Eng.*, 195(37–40), 5115–5140.
- Borja, R. I., and Koliji, A. (2009). "On the effective stress in unsaturated porous continua with double porosity." *J. Mech. Phys. Solids*, 57(8), 1182–1193.
- Borja, R. I., Liu, X., and White, J. A. (2012a). "Multiphysics hillslope processes triggering landslides." *Acta Geotech.*, 7(4), 261–269.
- Borja, R. I., Song, X., Rechenmacher, A. L., Abedi, S., and Wu, W. (2013a). "Shear band in sand with spatially varying density." *J. Mech. Phys. Solids*, 61(1), 219–223.
- Borja, R. I., Song, X., and Wu, W. (2013b). "Critical state plasticity. Part VII: Triggering a shear band in variably saturated porous media." *Comput. Methods Appl. Mech. Eng.*, 261–262, 66–82.
- Borja, R. I., and White, J. A. (2010a). "Conservation laws for coupled hydromechanical processes in unsaturated porous media: Theory and implementation." *Mechanics of Unsaturated Geomaterials*, L. Laloui, ed., John Wiley & Sons, New York, 185–208.
- Borja, R. I., and White, J. A. (2010b). "Continuum deformation and stability analyses of a steep hillside slope under rainfall infiltration." *Acta Geotech.*, 5(1), 1–14.
- Borja, R. I., White, J. A., Liu, X., and Wu, W. (2012b). "Factor of safety in a partially saturated slope inferred from hydro-mechanical continuum modeling." *Int. J. Numer. Anal. Methods Geomech.*, 36(2), 236–248.
- Burstedde, C., Wilcox, L. C., and Ghattas, O. (2011). "p4est: Scalable algorithms for parallel adaptive mesh refinement on forests of octrees." *SIAM J. Sci. Comput.*, 33(3), 1103–1133.
- Burton, G., Sheng, D., and Campbell, C. (2014). "Bimodal pore size distribution of a high-plasticity compacted clay." *Géotechnique Lett.*, 4, 88–93.
- Buscarera, G., and Einav, I. (2012). "The yielding of brittle unsaturated granular soils." *Géotechnique*, 62(2), 147–160.
- Callari, C., and Federico, F. (2000). "FEM validation of a double porosity elastic model for consolidation of structurally complex clayey soils." *Int. J. Numer. Anal. Methods Geomech.*, 24(4), 367–402.
- Carminati, A., et al. (2007). "Water flow between soil aggregates." *Transp. Porous Media*, 68(2), 219–236.
- Carreiro, J. F. (2009). "Numerical simulations on the influence of matrix diffusion to carbon sequestration in double porosity fissured aquifers." *Int. J. Greenhouse Gas Control*, 3(4), 431–443.
- Casini, F., Vaunat, J., Romero, E., and Desideri, A. (2012). "Consequences on water retention properties of double-porosity features in a compacted silt." *Acta Geotech.*, 7(2), 139–150.
- Della Vecchia, G., Dieudonné, A.-C., Jommi, C., and Charlier, R. (2015). "Accounting for evolving pore size distribution in water retention models for compacted clays." *Int. J. Numer. Anal. Methods Geomech.*, 39(7), 702–723.
- Della Vecchia, G., and Romero, E. (2013). "A fully coupled elastic-plastic hydromechanical model for compacted soils accounting for clay activity." *Int. J. Numer. Anal. Methods Geomech.*, 37(5), 503–535.
- Durner, W. (1994). "Hydraulic conductivity estimation for soils with heterogeneous pore structure." *Water Resour. Res.*, 30(2), 211–223.
- Dykhuzen, R. C. (1987). "Transport of solutes through unsaturated fractured media." *Water Res.*, 21(12), 1531–1539.
- Dykhuzen, R. C. (1990). "A new coupling term for dual-porosity models." *Water Resour. Res.*, 26(2), 351–356.
- Elsworth, D., and Bai, M. (1992). "Flow-deformation response of dual-porosity media." *J. Geotech. Eng.*, 10.1061/(ASCE)0733-9410(1992)118:1(107), 107–124.
- Feda, J. (1998). "Fragmentary clay—A difficult waste material." *Engineering geology*, 51(2), 77–88.
- Foster, C. D., and Mohammad Nejad, T. (2013). "Embedded discontinuity finite element modeling of fluid flow in fractured porous media." *Acta Geotech.*, 8(1), 49–57.
- Frey, J., Chambon, R., and Dascalu, C. (2013). "A two-scale poromechanical model for cohesive rocks." *Acta Geotech.*, 8(2), 107–124.
- Fuentes, I., Seguel, O., and Casanova, M. (2013). "Shear strength of aggregates compared with bulk soil of two haploxyerolls from Chile." *J. Soil Sci. Plant Nutr.*, 13(4), 819–831.
- Gallipoli, D., Wheeler, S. J., and Karstunen, M. (2003). "Modelling the variation of degree of saturation in a deformable unsaturated soil." *Géotechnique*, 53(1), 105–112.
- Gauden, P. A., Terzyk, A. P., Jaroniec, M., and Kowalczyk, P. (2007). "Bimodal pore size distributions for carbons: Experimental results and computational studies." *J. Colloid Interface Sci.*, 310(1), 205–216.
- Gerke, H. H. (2006). "Preferential flow descriptions for structured soils." *J. Plant Nutr. Soil Sci.*, 169(3), 382–400.
- Gerke, H. H., and van Genuchten, M. T. (1993a). "A dual-porosity model for simulating the preferential movement of water and solutes in structured porous media." *Water Resour. Res.*, 29(2), 305–319.
- Gerke, H. H., and van Genuchten, M. T. (1993b). "Evaluation of a first-order water transfer term for variably saturated dual-porosity flow models." *Water Resour. Res.*, 29(4), 1225–1238.
- Haggerty, R., and Gorelick, S. M. (1995). "Multiple-rate mass transfer for modeling diffusion and surface reactions in media with pore-scale heterogeneity." *Water Resour. Res.*, 31(10), 2383–2400.
- Hall, M. R., Mooney, S. J., Sturrock, C., Matelloni, P., and Rigby, S. P. (2013). "An approach to characterisation of multi-scale pore geometry

- and correlation with moisture storage and transport coefficients in cement-stabilised soils." *Acta Geotech.*, 8(1), 67–79.
- Heroux, M. A., and Willenbring, J. M. (2012). "A new overview of the Trilinos project." *Sci. Program.*, 20(2), 83–88.
- Howell, J. S., and Walkington, N. J. (2011). "Inf-sup conditions for twofold saddle point problems." *Numerische Mathematik*, 118(4), 663–693.
- Hu, L. B., Péron, H., Hueckel, T., and Laloui, L. (2013). "Desiccation shrinkage of non-clayey soils: Multiphysics mechanisms and a micro-structural model." *Int. J. Numer. Anal. Methods Geomech.*, 37(12), 1761–1781.
- Jarvis, N. J. (2007). "A review of non-equilibrium water flow and solute transport in soil macropores: Principles, controlling factors and consequences for water quality." *Eur. J. Soil Sci.*, 58(3), 523–546.
- Katsuki, D., Gutierrez, M., and Almrabat, A. (2014). "Stress-dependent elastic wave velocity of microfractured sandstone." *Int. J. Numer. Anal. Methods Geomechanics*, 38(5), 441–456.
- Kazemi, H., Merrill, L., Jr., Porterfield, K., and Zeman, P. (1976). "Numerical simulation of water-oil flow in naturally fractured reservoirs." *SPE J.*, 16(6), 317–326.
- Khalili, N., and Selvadurai, A. P. S. (2003). "A fully coupled constitutive model for thermo-hydro-mechanical analysis in elastic media with double porosity." *Geophys. Res. Lett.*, 30(24), 2268
- Köhne, J. M., Mohanty, B. P., Simunek, J., and Gerke, H. H. (2004). "Numerical evaluation of a second-order water transfer term for variably saturated dual-permeability models." *Water Resour. Res.*, 40(7), W07409.
- Koliji, A., et al. (2008). "Assessment of structural evolution of aggregated soil using neutron tomography." *Water Resour. Res.*, 44(5), W00C07.
- Koliji, A., Laloui, L., Cusinier, O., and Vulliet, L. (2006). "Suction induced effects on the fabric of a structured soil." *Transp. Porous Media*, 64(2), 261–278.
- Koliji, A., Laloui, L., and Vulliet, L. (2010a). "Constitutive modeling of unsaturated aggregated soils." *Int. J. Numer. Anal. Methods Geomech.*, 34(17), 1846–1876.
- Koliji, A., Vulliet, L., and Laloui, L. (2010b). "Structural characterization of unsaturated aggregated soil." *Can. Geotech. J.*, 47(3), 297–311.
- Lamb, A. R., Gorman, G. J., and Elsworth, D. (2013). "A fracture mapping and extended finite element scheme for coupled deformation and fluid flow in fractured porous media." *Int. J. Numer. Anal. Methods Geomech.*, 37(17), 2916–2936.
- Lewandowska, J., and Auriault, J. (2013). "Extension of Biot theory to the problem of saturated microporous elastic media with isolated cracks or vugs." *Int. J. Numer. Anal. Methods Geomech.*, 37(16), 2611–2628.
- Lewandowska, J., Ngoc, T. T., Vauclin, M., and Bertin, H. (2008). "Water drainage in double porosity soils: Experiments and micromacro modeling." *J. Geotech. Eng.*, 134(2), 231–243.
- Lewandowska, J., Szymkiewicz, A., Burzyński, K., and Vauclin, M. (2004). "Modeling of unsaturated water flow in double porosity soils by the homogenization approach." *Adv. Water Resour.*, 27(3), 283–296.
- Lewandowska, J., Szymkiewicz, A., Gorczewska, W., and Vauclin, M. (2005). "Infiltration in a double-porosity medium: Experiments and comparison with a theoretical model." *Water Resour. Res.*, 41(2), W02022.
- Lewis, R. W., and Ghafouri, H. R. (1997). "A novel finite element double porosity model for multiphase flow through deformable fractured porous media." *Int. J. Numer. Anal. Methods Geomech.*, 21(11), 789–816.
- Li, L., Meng, Q., Wang, S., Li, G., and Tang, C. (2013). "A numerical investigation of the hydraulic fracturing behaviour of conglomerate in glauconite formation." *Acta Geotech.*, 8(6), 597–618.
- Li, X., and Zhang, L. M. (2009). "Characterization of dual-structure pore-size distribution of soil." *Can. Geotech. J.*, 46(2), 129–141.
- Liu, C., and Muraleetharan, K. K. (2012a). "Coupled hydro-mechanical elastoplastic constitutive model for unsaturated sands and silts. I: Formulation." *Int. J. Geomech.*, 12(3), 239–247.
- Liu, C., and Muraleetharan, K. K. (2012b). "Coupled hydro-mechanical elastoplastic constitutive model for unsaturated sands and silts. II: Integration, calibration, and validation." *Int. J. Geomech.*, 12(3), 248–259.
- Liu, E., Yu, H. S., Deng, G., Zhang, J., and He, S. (2014). "Numerical analysis of seepage-deformation in unsaturated soils." *Acta Geotech.*, 9(6), 1045–1058.
- Mašin, D. (2013). "Double structure hydromechanical coupling formalism and a model for unsaturated expansive clays." *Eng. Geol.*, 165, 73–88.
- Miller, G. A., Khoury, C. N., Muraleetharan, K. K., Liu, C., and Kibbey, T. C. G. (2008). "Effects of soil skeleton deformations on hysteretic soil water characteristic curves: Experiments and simulations." *Water Resour. Res.*, 44(5), W00C06.
- Moench, A. (1984). "Double porosity models for a fissured groundwater reservoir with fracture skin." *Water Resour. Res.*, 20(7), 831–846.
- Mohammadnejad, T., and Khoei, A. R. (2013). "Hydro-mechanical modeling of cohesive crack propagation in multiphase porous media using the extended finite element method." *Int. J. Numer. Anal. Methods Geomech.*, 37(10), 1247–1279.
- Murad, M. A., and Loula, A. F. D. (1994). "On stability and convergence of finite element approximations of Biot's consolidation problem." *Int. J. Numer. Methods Eng.*, 37(4), 645–667.
- Musso, G., Romero, E., and Vecchia, G. D. (2013). "Double-structure effects on the chemo-hydro-mechanical behaviour of a compacted active clay." *Géotechnique*, 63(3), 206–220.
- Najser, J., Mašin, D., and Boháč, J. (2012). "Numerical modelling of lumpy clay landfill." *Int. J. Numer. Anal. Methods Geomech.*, 36(1), 17–35.
- Najser, J., Pooley, E., Springman, S. M., Laue, J., and Boháč, J. (2010). "Mechanisms controlling the behaviour of double porosity clay fills: In situ and centrifuge study." *Q. J. Eng. Geol. Hydrogeol.*, 43(2), 207–220.
- Nur, A., and Byerlee, J. D. (1971). "An exact effective stress law for elastic deformation of rock with fluids." *J. Geophys. Res.*, 76(26), 6414–6419.
- Nuth, M., and Laloui, L. (2008). "Effective stress concept in unsaturated soils: Clarification and validation of a unified framework." *Int. J. Numer. Anal. Methods Geomech.*, 32(7), 771–801.
- Rahman, M. M., and Rahman, S. S. (2013). "Fully coupled finite-element-based numerical model for investigation of interaction between an induced and a preexisting fracture in naturally fractured poroelastic reservoirs: Fracture diversion, arrest, and breakout." *Int. J. Geomech.*, 13(4), 390–401.
- Rahman, M. M., and Rahman, S. S. (2013). "Studies of hydraulic fracture-propagation behavior in presence of natural fractures: Fully coupled fractured-reservoir modeling in poroelastic environments." *Int. J. Geomech.*, 13(6), 809–826.
- Raj, M., and Sengupta, A. (2014). "Rain-triggered slope failure of the railway embankment at Malda, India." *Acta Geotech.*, 9(5), 789–798.
- Rohan, E., Naili, S., Cimrman, R., and Lemaire, T. (2012). "Multiscale modeling of a fluid saturated medium with double porosity: Relevance to the compact bone." *J. Mech. Phys. Solids*, 60(5):857–881.
- Romero, E., Della Vecchia, G., and Jommi, C. (2011). "An insight into the water retention properties of compacted clayey soils." *Géotechnique*, 61(4), 313–328.
- Romero, E., Gens, A., and Lloret, A. (1999). "Water permeability, water retention and microstructure of unsaturated compacted Boom clay." *Eng. Geol.*, 54(1–2), 117–127.
- Rotisciani, G. M., Sciarra, G., Casini, F., and Desideri, A. (2015). "Hydro-mechanical response of collapsible soils under different infiltration events." *Int. J. Numer. Anal. Methods Geomech.*, 39(11), 1212–1234.
- Sarma, P., and Aziz, K. (2006). "New transfer functions for simulation of naturally fractured reservoirs with dual porosity models." *SPE J.*, 11(3), 328–340.
- Shen, W., He, Z., Dormieux, L., and Kondo, D. (2014). "Effective strength of saturated double porous media with a Drucker–Prager solid phase." *Int. J. Numer. Anal. Methods Geomech.*, 38(3), 281–296.
- Šimůnek, J., Jarvis, N. J., van Genuchten, M. T., and Gardenas, A. (2003). "Review and comparison of models for describing non-equilibrium and preferential flow and transport in the vadose zone." *J. Hydrol.*, 272(1), 14–35.
- Song, X., and Borja, R. I. (2014a). "Finite deformation and fluid flow in unsaturated soils with random heterogeneity." *Vadose Zone J.*, 13(5).
- Song, X., and Borja, R. I. (2014b). "Mathematical framework for unsaturated flow in the finite deformation range." *Int. J. Numer. Methods Eng.*, 97(9), 658–792.
- Svanadze, M., and Scalia, A. (2013). "Mathematical problems in the coupled linear theory of bone poroelasticity." *Comput. Math. Appl.*, 66(9), 1554–1566.
- Terzaghi, K. (1943). *Theoretical Soil Mechanics*, Wiley, New York.

- Tjioe, M., and Borja, R. I. (2015). "On the pore-scale mechanisms leading to brittle and ductile deformation behavior of crystalline rocks." *Int. J. Numer. Anal. Methods Geomech.*, 39(11), 1165–1187.
- van Genuchten, M. T. (1980). "A closed-form equation for predicting the hydraulic conductivity of unsaturated soils." *Soil Sci. Soc. Am.*, 44(5), 892–898.
- Varnes, D. (1978). "Slope movement types and processes." *Landslides Analysis and Control*. Special Rep. 176, National Academy of Sciences, Washington, DC.
- Venegas, R., and Umnova, O. (2011). "Acoustical properties of double porosity granular materials." *J. Acoust. Soc. Am.*, 130(5), 2765–2776.
- Vitone, C., Cotecchia, F., Viggiani, G., and Hall, S. (2013a). "Strain fields and mechanical response of a highly to medium fissured bentonite clay." *Int. J. Numer. Anal. Methods Geomech.*, 37(11), 1510–1534.
- Vitone, C., Viggiani, G., Cotecchia, F., and Hall, S. (2013b). "Localized deformation in intensely fissured clays studied by 2D digital image correlation." *Acta Geotech.*, 8(3), 247–263.
- Vu, M. N., Pouya, A., and Seyedi, D. M. (2014). "Theoretical and numerical study of the steady-state flow through finite fractured porous media." *Int. J. Numer. Anal. Methods Geomech.*, 38(3), 221–235.
- Warren, J., and Root, P. (1963). "The behavior of naturally fractured reservoirs." *SPE J.*, 3(3), 245–255.
- Weng, X., Kresse, O., Cohen, C., Wu, R., and Gu, H. (2011). "Modeling of hydraulic-fracture-network propagation in a naturally fractured formation." *SPE Prod. Oper.*, 26(4), 368–380.
- White, J. A., and Borja, R. I. (2008). "Stabilized low-order finite elements for coupled solid-deformation/fluid-diffusion and their application to fault zone transients." *Comput. Methods Appl. Mech. Eng.*, 197(49–50), 4353–4366.
- White, J. A., and Borja, R. I. (2011). "Block-preconditioned Newton–Krylov solvers for fully coupled flow and geomechanics." *Comput. Geosci.*, 15(4), 647–659.
- White, J. A., et al. (2014). "Geomechanical behavior of the reservoir and caprock system at the In Salah CO₂ storage project." *PNAS*, 111(24), 8747–8752.
- Yang, X., Richmond, M. C., Scheibe, T. D., Perkins, W. A., and Resat, H. (2014). "Flow partitioning in fully saturated soil aggregates." *Transp. Porous Media*, 103(2), 295–314.
- Yin, S. (2013). Numerical analysis of thermal fracturing in subsurface cold water injection by finite element methods." *Int. J. Numer. Anal. Methods Geomech.*, 37(15), 2523–2538.
- Zhang, J., and Roegiers, J. C. (2005). "Double porosity finite element method for borehole modeling." *Rock Mech. Rock Eng.*, 38(3), 217–242.
- Zhang, S., Yin, S., and Yuan, Y. (2015). "Estimation of fracture stiffness, in situ stresses, and elastic parameters of naturally fractured geothermal reservoirs." *Int. J. Geomech.*, 15(1), 04014033.
- Zimmerman, R. W., Chen, G., Hadgu, T., and Bodvarsson, G. S. (1993). "A numerical dual-porosity model with semianalytical treatment of fracture/matrix flow." *Water Resour. Res.*, 29(7), 2127–2137.